2024

A Biofilm Channel Origin for Vermiform Microstructure in Carbonate Microbialites

Yadira Ibarra

Pedro J. Marenco

Jakob P. Centlivre

Brain P. Hedlund

Laura K. Rademacher

See next page for additional authors

Authors

Yadira Ibarra, Pedro J. Marenco, Jakob P. Centlivre, Brain P. Hedlund, Laura K. Rademacher, Sarah E. Greene, David J. Bottjer, and Frank A. Corsetti

A biofilm channel origin for vermiform microstructure in carbonate microbialites

Yadira Ibarra[1]*, Pedro J. Marenco[2], Jakob P. Centlivre[3], Brian P. Hedlund[3], Laura K. Rademacher[4], Sarah E. Greene[5], David J. Bottjer[6], Frank A. Corsetti[6]

[1] *School of the Environment, San Francisco State University, San Francisco, CA, 94132, USA*

[2] *Department of Geology, Bryn Mawr College, Bryn Mawr, PA 19010, USA*

[3]*School of Life Sciences, University of Nevada, Las Vegas, Nevada 89154-4004, USA*

[4]*Geological and Environmental Sciences, University of the Pacific, Stockton, CA 95211, USA*

[5] *School of Geography, Earth and Environmental Sciences, University of Birmingham, Edgbaston, Birmingham, B15 2TT, UK*

[6] *Department of Earth Science, University of Southern California, Los Angeles, CA, 90089, USA*

*Corresponding author: yibarra@sfsu.edu

Keywords: microbialites; taphonomy; microfossils; biofilms; carbonates

Competing Interest Statement: No competing interests to disclose.

Acknowledgements

We thank Patrick Browning and Connor Penrod for field assistance and access support in the Springs Mountains Nevada under permit number SMA0463. Financial support was provided by NSF EAR 2038374 to Y.I., NSF EAR 2038420 to B.P.H., and NSF EAR 2038377 to L.K.R. P.J.M. was supported by NSF award EAR 2221249.

ABSTRACT

A three-dimensional tubular fabric known as ‘vermiform microstructure’ in Phanerozoic and Neoproterozoic carbonate microbialites has been hypothesized to represent the body fossil of nonspicular keratose demosponges. If correct, this interpretation extends the sponge body fossil

record and origin of animals to ~890 Ma. However, the veracity of the keratose sponge interpretation for vermiform microstructure remains in question and the origin of the tubular fabric is enigmatic. Here we compare exceptionally well-preserved microbialite textures from the Upper Triassic to channel networks created by modern microbial biofilms. We demonstrate that anastomosing channel networks of similar size and geometries are produced by microbial biofilms in the absence of sponges, suggesting the origin for vermiform microstructure in ancient carbonates is not unique to sponges and perhaps best interpreted conservatively as likely microbial in origin. We present a taphonomic model of early biofilm lithification in seawater with anomalously high carbonate saturation necessary to preserve delicate microbial textures. This work has implications for the understanding of three-dimensional biofilm architecture that goes beyond the current micro-scale observations available from living biofilm experiments, and suggests that biofilm channel networks have an extensive fossil record.

1 INTRODUCTION

Characterization of morphologic attributes of fossilized organisms remains one of the most common methods of assigning taxonomic affinities to ancient and extinct organisms (Hopkins & Gerber, 2020). However, taphonomic biases and morphologic similarities among fossil groups often complicate accurate taxonomic identification (Brasier *et al.*, 2011; Anderson *et al.*, 2023). In instances when fossil or fossil-like remains contain parts resembling multiple taxonomic groups, assigning taxonomic affinities can be particularly challenging, especially for organisms whose body parts or community structure lack symmetry, like sponges and microbial constructions (Mehra *et al.*, 2020).

An anastomosing meshwork of microspar-filled tubules of varied diameter known as ‘vermiform microstructure’, found in ancient microbialites and once considered microbial in

origin (Walter, 1972), has more recently been interpreted to represent keratose (non-spicular) sponges (Lee *et al.*, 2014; Luo & Reitner, 2014). This work has led to new reports of interpreted sponge body fossils in ancient carbonate microbialites including vermiform microstructure in reefs from ~890 Ma (Turner, 2021), thus potentially predating the oldest uncontroversial sponge body fossils (Antcliffe *et al.*, 2014) by ~350 million years. The lack of scientific consensus on methodologies to distinguish between keratose sponge fossils and microbial textures remains problematic in their use to reconstruct past environments and reflect accurate evolutionary transitions (Kershaw *et al.*, 2021; Neuweiler *et al.*, 2023). Furthermore, recent experiments with extant microbial biofilms reveal similar vermiform geometries in the absence of sponges (Wilking *et al.*, 2013; Zhang *et al.*, 2018). Here, we use an exceptionally well-preserved microbialite from the rock record as a morphologic analog for a range of vermiform geometries increasingly attributed to keratose sponge body fossils, and suggest an alternative interpretation for the origin and taphonomy of vermiform microstructure.

2 THE COTHAM MARBLE AS A MORPHOLOGIC ANALOG FOR VERMIFORM MICROSTRUCTURE

The Upper Triassic Cotham Member of the Lilstock Formation of the southwestern United Kingdom contains laterally extensive stromatolitic and dendrolitic carbonate microbialite mounds (~20 cm thick, decimeters to meters in diameter) known as the Cotham Marble (CM) (Hamilton, 1961; Wright & Mayall, 1981). The CM microbialites were deposited in the shallow Tethys sea between Gondwana and Laurasia during a marine transgression on a shallow storm-dominated carbonate ramp that alternated between periods of restriction and connection to open marine waters (Hesselbo *et al.*, 2004). The CM coincides with the end-Triassic mass extinction interval (Ibarra *et al.*, 2016) and led to the oldest non-skeletal marine seasonal temperature

71 record (Petryshyn *et al.*, 2020). Traceable laminated and dendrolitic phases of the CM across
72 individual microbialite mounds indicate a strong environmental control on microscopic microbial
73 features (Ibarra *et al.*, 2015; Ibarra & Corsetti, 2016). The microbialites are associated with an
74 inter-mound, channel, flat-pebble conglomerate facies that formed from current reworking before
75 lithification (Hamilton, 1961).

76 Petrographic observations of the CM microbialites reveal vermiform geometries that are
77 strikingly similar to the texture and fabric of vermiform microstructure from Phanerozoic and
78 Neoproterozoic microbialites (Figure 1). Figure 1a compares the vermiform microstructure of
79 *Madiganites mawsoni* (Figure 1a; Walter, 1972) to textures in the first laminated layer (L1 in
80 Ibarra et al., 2014) of the CM microbialites (Figures 1b-c). The bright, narrow, sinuous areas are
81 composed of microsparitic calcite, while the darker regions are composed of micrite (Figure 1c).
82 Figures 1d-k illustrate similarities in texture between the CM and textures from the geologic
83 record where the vermiform geometries are interpreted as the spongin network of keratose
84 sponges. Basal stromatolitic laminations that comprise the lowermost laminated layer of the CM
85 contain a tubular fabric (Figures 1d-e) that resembles the texture, size, and branching nature of
86 vermiform geometries in Cambrian *Cryptozoon* stromatolites (compare Figure 1d to Figure 1f;
87 Lee & Riding, 2021) and in Upper Cambrian maze-like reefs (compare Figure 1e to Figure 1g;
88 Lee et al., 2014). The tubular fabric is also present in the interdendrolite fill of the dendrolitic
89 phases of the CM (Figure 1h) as well as *within* the dendrolites (see arrows in Figure 1i).
90 Comparable tubular fabrics to Figures 1h-i of the CM have been described from Upper
91 Ordovician micritic limestones (compare Figure 1h to Figure 1j; Park *et al.*, 2015) and
92 Neoproterozoic reefs (compare Figure 1i to Figure 1k; Turner, 2021). Given the petrographic
93 similarities (Figure 1) between the tubular fabric in the CM and vermiform microstructures from

the geologic record—interpreted as the permineralized spongin skeletal structure of keratose sponges (Lee *et al.*, 2014; Luo & Reitner, 2014; Park *et al.*, 2015; Lee & Riding, 2021),—we present a detailed description of the scales and variability of vermiform geometries in the CM and its associated facies (e.g., flat-pebble conglomerate) to provide clarity on the origin and taphonomy of seemingly identical enigmatic microstructures (Figure 1).

3 MATERIALS AND METHODS

3.1 Ancient and modern geologic samples

This work primarily focuses on detailed descriptions of petrographic fabrics containing different scales of vermiform geometries of Triassic CM samples from Bristol, Manor Farm, Stowey Quarry, and Lower Woods (see Appendix S1 Figure S1 for map of sites). We then compare the textures in the CM to similar geometries created in modern biofilms from the literature. Finally, we present a novel taphonomic model for the creation of vermiform microstructure using Recent freshwater carbonates from the Spring Mountains of Nevada, and examples from the geologic record (Ordovician mudmounds and microbialites of the Neoproterozoic Noonday Dolomite).

3.2 Definition and significance of tubule diameter

Vermiform microstructure is defined as a type of laminar architecture that consists of narrow, sinuous, pale-colored areas (usually sparry carbonate) surrounded by darker, usually fine-grained areas (usually micrite) (Walter, 1972; Grey & Awramik, 2020). In this text, we refer to the narrow, sinuous, sparry regions as ‘tubules’ for their cylindrical morphology that in many instances, display round-cross-sections (Figure 1h), thus revealing their cylindrical (i.e.,) three-dimensional morphology. Vermiform microstructure can be distinguished from similarly preserved ‘rectilinear’ network fabrics composed of mostly criss-crossing straight lines of sparite

with nodes interpreted as spiculate sponges (see Figures 3 and 5 in Neuweiler *et al*., 2023). In this study, tubule diameter refers to the width of the sparry tubule. We note that the tubule diameter can vary slightly for a single tubule and thus use the terms 'nearly-uniform' or 'nearly consistent' diameter in reference to slight deviations from tubule uniformity.

While tubule diameter in the CM is variable, it is important to note that keratose spongin fibers—the rigid skeleton part of keratose sponges that has been attributed to vermiform microstructure—also exhibit diameter variability and size variability (Jesionowski *et al.*, 2018; Stocchino *et al.*, 2021). Nonetheless, the relative tubule uniformity between CM vermiform structures, biofilm channels (discussed in section 5.2), and known sponge fossils is notable. Although tubule diameter is a criteria used to attribute vermiform microfabric to a sponge origin, it is not diagnostic and other lines of evidence (such as macrostructure shape, tubule arrangement) must be used to ascertain biologic affinities (Luo *et al.*, 2022; Neuweiler *et al.*, 2023). In this text, we use measurements of tubule diameters as a means of comparing to other reports of vermiform microstructure from the literature.

3.3 Tubule diameter measurements

Tubule diameter measurements were produced using image processing software (ImageJ; http://imagej.nih.gov/ (Appendix S1 Figures S2-S6 and Tables S1-S3). Photomicrographs containing vermiform microstructure were binarized to highlight pixel intensity differences between dark (micritic) pixels and light (sparitic vermiform) pixels. The average tubule diameters were estimated using the Otsu thresholding method (Otsu *et al.*, 1979), which finds the optimal threshold based on the grayscale intensity values of the image pixels. The number of tubules, and the minor-axis of a best-fit ellipse for each tubule was quantified using the particle counting feature in ImageJ software with a particle size limit between 100 μm^2 and 10,000 μm^2.

4 RESULTS

4.1 Description of different scales of vermiform microstructure in the CM microbialites

The basal layer of the CM microbialites is comprised of micritic laminae (labeled "L1" in Ibarra *et al*., 2014). Vermiform fabrics occur along laminar bands ~5 mm thick (Figures 2a-c) and are microstratigraphically succeeded by fenestral fabrics typical of laminoid fenestrae (Tebbutt *et al.*, 1965; Choquette & Pray, 1970; Figure 2d) and fenestral pores that form the axial zones of conical lamina (Ibarra et al., 2014; Figure 2e). The tubules display an anastomosing pattern (Figures 2f-g) and share similar microspar-filling cements with adjacent fenestral fabrics (compare Figures 2d, e, and g). Measurements of tubule diameters in the CM resembling examples from the literature (e.g., Figure 1) are variable across all facies examined, with an average diameter of approximately 40 μm (36.5 ± 22 μm, n=374; Figure S2 and Table S1) and are composed of microspar separated by peloidal micritic aggregates that are ~50-100 μm in diameter (Figures 2c, f-g).

Dendrolitic layers of the CM microbialites (labeled "D1" and "D2" in Ibarra et al., 2014) exhibit remarkably evenly spaced (~150 μm in diameter) microbial branching patterns (Ibarra *et al.*, 2014, 2015) resulting in inter-dendrolite spacing that is filled with sparry cement or micrite ("f" in Figure 3a). Bedding plane cross sections of the dendrolitic regions ("d") further highlight the bifurcating nature and diameter uniformity of the spacing between the dendrolite 'branches' (Figure 3b). In other instances, oblique cross-sections of polished slabs reveal the same branching tubular and semi-round cross-sections of inter-dendrolite spaces with an average diameter of approximately 150 μm (149.32 ± 73.16 μm, n=104; Figure 3c-d and Figures S3-S4). These round to elliptical fenestrae are interpreted to result from early-lithified, evenly spaced, three-dimensional (3D) branching in microbial mats that result in round to elliptical voids when

represented in two dimensions (Ibarra *et al*., 2014). High-resolution scans of the dendrolites reveal a network of submillimeter-scale branching tubules that prominently cap the upper regions of the dendrolites (Figures 3e-h). Detail of the internal structure of the dendrolites is shown in Figure 4, revealing the petrographic features of the network of branching tubules.

Many of the upper regions of the dendrolite branches are composed of what have been described as peloidal micritic fabrics (Ibarra *et al*., 2014), where the micritic aggregates are separated by microspar-filled anastomosing tubules (Figures 4b-d). While most dendrolites exhibit a laminated micritic texture (Ibarra *et al*., 2014), some are composed of peloidal micrite that is separated by an evenly spaced, microsparitic, tubular network (Figure 4). The tubules anastomose within the dendrolitic structures (Figure 4b-f), and strongly resemble the shape, size, and texture of vermiform geometries found in the basal laminated layers (Figure 2c). However, the preservation of the tubule structures is highly variable, such that some dendrolitic regions contain vermiform geometries where the tubules exhibit smaller-than-average diameters with distinct circular cross-sections (~10 μm in diameter), somewhat resembling a 3D stitch pattern (Figures 4e-f). Micritic intra-dendrolite regions contain conspicuous pyrite-coated filamentous structures (black specs in Figure 4b) interpreted as possible microfossils whose pyrite composition was confirmed using a scanning electron microscope (SEM) coupled with energy dispersive spectroscopy (EDS) (Ibarra *et al.*, 2014). Figure 4g summarizes the tubule diameter estimates for L1 and D1 facies of the CM microbialites and for the larger inter-dendrolite fenestra (Appendix S1 Figures S2, S3, and S4).

Vermiform geometries from the dendrolitic phases of the CM predominantly occur within the dendrolites, but there are rare examples where vermiform microstructures occur in micritic regions *between* the dendrolites (Figure 5). This inter-dendrolite micrite develops on and

186 adjacent to the dendrolites (Figures 5b-d), suggesting a less-dense continuation of growth from
187 the dendrolite structures as is evidenced by the rounded protrusions that resemble the dendrolite
188 morphology (Figure 5d) and the presence of bridging structures (*sensu* Marenco *et al.*, 2002;
189 Corsetti & Grotzinger, 2005) that connect adjacent dendrolite 'branches' (Figure 5b). Vermiform
190 microstructures of variable geometries that display distinct circular cross-sections (small arrows
191 near bottom of Figure 5d) occur in the inter-dendrolite micrite and are excluded from the
192 microspar fill regions (Figure 5b-d). In a rare example, an isolated dendrolitic 'branch' with a
193 sharp linear boundary on one side was detected in the fill region (Figure 5e-f). The dendrolitic
194 structure displays a well-preserved network of vermiform fabric as well as an internal larger
195 (~150 μm diameter) ovoid cross-section denoted by the central arrows (Figure 5f).
196 The CM microbialites are remarkably laterally extensive, whereby millimeter-scale
197 features can be traced across their respective meter-scale mounds at different locations and up to
198 ~100 km away from one another (Ibarra and Corsetti, 2016). Here we demonstrate that the
199 vermiform fabric associated with the dendrolitic phases can similarly be traced from site to site
200 (Figure 6), suggesting an element of regional control on its development.
201 We also examined a flat-pebble conglomerate unit associated with the CM microbialites
202 that resulted from current reworking in channels that separated the meter-scale mounds
203 (Hamilton, 1961). The low sphericity flat-pebble clasts ("p") can be up to ~8 cm long and are
204 composed of fine-grained carbonate (Figures 7a-c). Previous studies demonstrated that some of
205 the clasts act as nucleation surfaces for dendrolitic structures (Hamilton, 1961). Indeed,
206 petrographic analyses of flat-pebble clasts reveal millimeter-scale micritic growths that develop
207 on, and in some cases form fringes around the pebble, somewhat resembling the dendrolitic
208 phases of the CM in their micritic nature and domed morphology (see arrows in Figure 7a and

protrusion petrographic detail in Figures 7b-c). The domical microdigitate protrusions have a semi-layered microstructure (Figure 7d), but are better classified as having a clotted (Shapiro, 2000) micritic internal texture separated by microsparitic tubules that anastomose in the micritic framework, resembling the vermiform fabric described in the laminated and dendrolitic phases of the CM (Figures 2 and 4). In addition to the microsparitic bifurcating tubule structures (~40 μm in diameter), larger sparry features resembling the inter-dendrolite spacing (~150 μm in diameter) from Figures 3b-c are also present in the flat-pebble facies (arrows in Figure 7c).

5 DISCUSSION

5.1 Assessing the possibility of sponges in the CM microbialites

Here we have demonstrated that the CM microbialites contain a diverse array of vermiform geometries from dendrolite, stromatolite, interdendrolite regions, and flat-pebble conglomerate facies that are remarkably similar in size (~40 micron diameter), shape (tubular with round cross-sections), branching nature (three-dimensional), and textural composition (microsparitic) to reported vermiform microstructures from the rock record increasingly interpreted as the remnants of keratose sponge bodies. Below we consider observations from this study to evaluate the possibility that vermiform geometries of the CM represent sponge body fossils.

5.1.1 Microfossil distribution

It is well-known that microbes inhabit sponge tissues (Taylor *et al.*, 2007), thus raising the possibility that the interpreted pyritic microfossils found in the micritic textures of the CM could be inhabitants of putative sponges. However, the pyritic fossil distribution is (1) restricted to micritic regions of the dendrolitic and laminated phases of the CM, and (2) does not scale to sponge morphologies (e.g., Botting, 2005). In order for keratose sponges to be preserved through

232 permineralization, at least somewhat of a mesoscopic body fossil should be produced that
233 preserves the shape of the relic sponge (Neuweiler et al., 2023) as has been demonstrated for
234 accepted examples of "sponge mummies" in lithisthids (Froget, 1976), hexactinellids, (Brachert
235 *et al.*, 1987) and non-lithistid demosponges (Ritterbush *et al.*, 2015). The distribution of pyrite
236 filaments within the micritic regions (Figure 4 and Ibarra et al., 2014) together with previously
237 reported elevated total organic carbon (TOC) for the dendrolites versus the inter-dendrolite fill
238 (Ibarra *et al*., 2014), indicates the pyrite structures are more likely microbial remnants associated
239 with the creation and/or degradation of the dendrolitic and micritic regions (Ibarra *et al*., 2014),
240 as opposed to lithified sponge tissue inhabitants.

241 *5.1.2 Lateral continuity of mm-scale features*

242 Vermiform microstructure has been shown to be laterally continuous for several meters
243 and its lateral continuity has been used as an argument against a possible sponge origin (Pratt,
244 1982). Here we demonstrate the lateral persistence of vermiform microstructure across individual
245 bioherms for samples collected up to ~50 km away from one another (Figure 6) suggesting a
246 large-scale control on its development (*sensu* Ibarra and Corsetti, 2016). While it is possible that
247 sponges may have been responding to large-scale environmental forcings, it seems unlikely that
248 some episodes of their development would (1) occur at precise 'stratigraphic levels' up to ~50
249 km apart, (2) be limited to a thickness of ~0.5 mm (e.g., Figure 6), and (3) conform to the bounds
250 of the preexisting dendritic morphology. On the cm-scale, the dendrolites of the CM are
251 remarkably consistent in their dendrolitic habit (Ibarra *et al*., 2014), however, their microfabric is
252 laminated or clotted (described here as vermiform) (Ibarra *et al*., 2014). If vermiform
253 microstructure is indeed reflective of a sponge origin in the CM, then the creation of the
254 dendrolites would be dependent upon the presence of spongin to give the dendrolites rigidity.

The absence of vermiform microstructure in many dendrolites and the occurrence of vermiform microstructure at precise stratigraphic levels (Figure 6), implies it is not integral to the formation of the dendrolites or in giving them rigidity. Thus, a more parsimonious explanation for the (1) the lateral continuity of mm-scale fabrics and (2) the presence and absence of vermiform microstructure in adjacent and within the same dendrolitic structure is that the dendrolites represent a microbial feature whose fabric (i.e., laminated versus vermiform) reflects a large-scale forcing.

5.1.3 Vermiform microstructure on flat-pebble clasts

Thus far, most examples of vermiform microstructure have come from observations in microbialites or reefs from restricted lagoons to open shelf settings (Neuweiler *et al*., 2023), and here we show the occurrence of vermiform geometries of two different diameters (~40 μm and ~150 μm) in a flat-pebble conglomerate facies representing shallow and possibly evaporative conditions (Hamilton, 1961). Flat-pebble conglomerates are known to form after the seafloor has been partially lithified, and subsequent storm events or other high-energy conditions, rip up the clasts and redeposit the lithified micrite (Sepkoski, 1982). Flat-pebble clasts associated with the Cotham Marble are interpreted as inter-microbialite mound channel deposits that occasionally are found in the inter-dendrolite fill of the microbialites (Hamilton, 1961). The fringing nature (Figure 7a) of the microdigitate structures implies they developed after the pebbles were ripped up and redeposited. The depositional setting (i.e., channel fill) and mm-scale morphology of the micrite (i.e., dendrolitic) suggest the micritic structures more likely represent the early development of microbial dendrolites like those of the CM, as opposed to lithified sponge bodies that colonized the fringes of flat-pebble clasts (Figure 7).

5.2 A new interpretation for vermiform microstructure: lithified biofilm channels

A recent review of interpreted keratose spongin preservation in the rock record summarizes key caveats in the sponge interpretation for vermiform microstructure (Neuweiler, *et al*., 2023). Most notably, there is no existing taphonomic pathway or model that can explain the permineralization of the spongin skeleton of a keratose sponge into microspar cement, while also mummifying the sponge body transforming it to homogenous fine-grained carbonate—all prior to compaction. While studies have questioned the spongin origin for vermiform microstructure (Kershaw *et al*., 2021), in the absence of a credible alternative hypothesis, the origin and taphonomy of vermiform microstructure remains an enigma. Below we propose a mechanism for the creation of vermiform microstructure that has yet to be considered in the vermiform microstructure debate, based on the diverse vermiform geometries and scale-dependent observations from the CM (centi-metric to micro-metric), together with observations from the literature on modern biofilms and Recent carbonate coated grains.

5.2.1 Biofilm channels

Modern biofilm experiments demonstrate the creation of an anastomosing, tubular geometry by microbial biofilms in the form of intra-biofilm water channels (Lawrence *et al.*, 1991; Costerton *et al.*, 1994; de Beer *et al.*, 1994; Stoodley *et al.*, 1994). In natural aquatic environments, surface-associated microbial communities are encased in a self-produced matrix of extracellular polymeric substances (EPS) that develop pores and interconnected channels (Lawrence *et al.*, 1991; Flemming & Wingender, 2010). These nutrient-poor regions are also known as EPS matrix voids and represent water-filled regions in biofilms that exist between and within microbial clusters (Flemming and Wingender, 2010). Biofilm channels can be distinguished from biofilm pores by their high length/width ratio (~ >10), whereas pores have length/width ratios that are closer to one (Quan *et al.*, 2022).

Studies on modern biofilm cultures indicate channel formation is process-driven and that channels serve specific functions within biofilms such as particle transport and distribution of nutrients (Rooney *et al.*, 2020). Wild-type *Bacillus subtilis* biofilms have been shown to produce highly interconnected, elongate, channel networks (with an average channel diameter of 91 ± 65 μm) that enhance the transport of liquids within biofilms (Wilking *et al.*, 2013). The formation of channels in colonies of *Pseudomonas aeruginosa* is governed by biofilm growth rate and adhesion of the film to the substrate (Geisel *et al.*, 2022). Channel networks in *Escherichia coli* biofilms indicate that intra colony channel morphologies are influenced by substrate composition and availability of nutrients (Bottura *et al.*, 2022).

Most studies that have been successful in imaging the shape and structure of biofilm pores and interconnected water channels have done so on relatively thin biofilms, due to the technological limitations of imaging thicker, more mature, hydrated biofilms (Yan *et al.*, 2016). These procedural constraints restrict the opportunity for biofilms to create more complex, 3D morphologies that may reveal the internal structural architecture of a mature biofilm. Similarly, field studies of living or recently-lithified, mixed-community, aquatic biofilms that would be more representative of natural environments typically lose their architectural properties once removed from their *in-situ* growth position.

The textures we describe in the CM are an example of an exceptionally well-preserved ancient microbialite that contains tubular fabrics that are similar in size, shape, and anastomosing nature to biofilm channels observed in microbial experiments (Figures 8a-c'). Reported channel diameters in extant microbial biofilms are within the range of tubule diameters found in vermiform microstructures from the CM (Figure 4g), but have highly variable widths (Lei *et al.*, 2020; Bottura *et al.*, 2022). Most imaging of biofilm channels has been on biofilm growth

observed on flat surfaces (e.g., agar plates or microfluidic conduits), thus giving channels somewhat parabolic cross-sections. As channels mature, they can develop circular cross-sections (Wilking *et al*., 2013) similar to the round-cross sections observed in many examples of vermiform microstructure (Figures 1h, 4f).

5.2.2 Three-dimensional tubular aspect of biofilm channels

On a two-dimensional (i.e., flat) plane, modern biofilms create diverse geometries that resemble vermiform microstructure from the rock record (Figure 8a-c'). However, vermiform tubule architecture is three-dimensional in its branching nature (Luo and Reitner, 2014), thus appearing to limit the applicability of their comparison to biofilm channels. In order for vermiform microstructure to possibly represent lithified biofilm channels, modern biofilm water channels must show evidence for anastomosis in three dimensions that create a meshwork of tubules with somewhat uniform diameters that exhibit circular cross-sections.

The 3D nature and tubular geometries of hydrated algal biofilm sediment aggregates (BSA) were recently observed using X-ray microcomputed tomography (μ-CT), which allows for the 3D visualization of fully hydrated biofilms without the need for desiccation (Zhang *et al*., 2018). The pore water component of the BSA is composed of 3D, tubular geometries that bifurcate and exhibit distinct circular cross-sections that are enveloped by biofilm (Figures 8d-f; Zhang et al., 2018). The sizes of the tubular water channels in the BSA are smaller (~5-10 μm in diameter)—yet still within the range of tubule diameters recorded in the CM (Figures 4g and 8g). While there is a slight difference in the tubule diameter size relative to the size of vermiform microstructure from the rock record (~5-10 μm versus ~ 40 μm), it is nonetheless intriguing that algal biofilms are able to create seemingly delicate water channels of nearly consistent diameter,

346 with complex, 3D branching, despite being enmeshed in detrital sediment, which could
347 potentially smother the thin tubular structures.
348 Biofilms growing in carbonate environments and cavities with limited to no detrital and
349 siliciclastic sedimentation are likely able to create increasingly complex water channel
350 morphologies that exhibit near-isotropic anastomosis such as those shown in vermiform
351 geometries of the CM. It has been shown, for example, that modern microbial mats reduce their
352 morphological complexity during times of increased mud deposition (Mackey *et al.*, 2017), and
353 the majority of vermiform geometries reported from the rock record were deposited in carbonate
354 environments with little to no detrital input (Neuweiler, et al., 2023), potentially allowing for the
355 development of increasingly complex biofilm channel microstructures.
356 One advantage of being able to observe the larger, mesoscopic architecture of the
357 dendrolites in the CM, is that a larger-scale (~150 μm diameter), tubular architecture displaying
358 anastomosis and circular cross-sections is revealed (Figures 3b-d). These larger-scale inter-
359 dendrolite fenestrae that emerge at the interface between dendrolite branches, may represent a
360 larger biofilm channel architecture that has yet to be described in modern laboratory-grown
361 biofilms, but is likely prevalent in natural aquatic substrates and possibly preserved in the
362 geologic record under the right geochemical and environmental conditions.
363 **5.3 A taphonomic model for vermiform microstructure**
364 The preservation of delicate tubular water channels within microbial biofilms necessitates
365 a taphonomic model that accounts for the creation of two distinct textures (micrite and adjacent
366 tubular microspar). We propose the micritic regions of vermiform geometries represent a
367 micrite-precipitating community of microbes in a dense EPS matrix (Decho *et al.*, 2005; Dupraz
368 & Visscher, 2005; Dupraz *et al.*, 2013), supported by the presence of possible microfossils

(Figures 4 and Ibarra et al., 2014), while the tubular bifurcating microspar represents the early (and likely syngenetic) precipitation of microspar cements within biofilm water channels or EPS-poor regions within the microbial structure (Figures 9a-c). In this model, the water channels transport and host supersaturated fluids with respect to calcite that ultimately precipitate sparry cements within them (Figure 9d), thus cementing and preserving the vermiform geometries (Figure 9e). Alternatively, scenarios may exist where the EPS portion of the biofilm becomes lithified, while the EPS-poor regions and water channels remain uncemented, but preserved as porous tubular cavities (Figure 9c'). Upon return to supersaturated fluids, the tubular cavities can become cemented by pore-occluding sparry cements (Figure 9d).

Observations from Recent coated grains collected from cold spring carbonate environments in the Spring Mountains of Nevada show the creation of similar vermiform geometries preserved as tubular porosity along laminar bands of freshwater carbonate oncoids (Figure 10a-i). The texture created by the tubular shapes of the pores along the laminar bands of the oncoids is known as Spongiostromate in the microbialite literature (Flügel, 2004), and is described as a very variable micritic, spongious, vermicular, fenestral, and peloidal texture (Gürich, 1906). Spongiostromate oncoids were common in Proterozoic marine platform settings (Flügel, 2004). Although the original description of Spongiostromate was used to describe a porous *microbial* texture (Gürich, 1906), the resemblance of Spongiostromate microstructure to vermiform microstructure led to the recent sponge interpretation of the Mississippian *Spongiostroma* fossils (Lee & Riding, 2022). In fact, observations from Recent freshwater oncoids, which bear strong textural resemblance to their Proterozoic counterparts, reveal an important taphonomic step that is not always discernible in the study of ancient microbialites. The porous network present in the Recent oncoids from Figure 10 suggest that the creation of

vermiform microstructure may involve a sequence of events that include (1) lithification of microbial EPS, followed by (2) the pore-occlusion of tubular cavities that may represent former intra-biofilm water channels or intra-biofilm EPS-poor regions (Figure 10). Estimates of tubule diameters do not show a statistically significant difference between L1 and D1 tubules in the CM microbialites and tubule pores in freshwater oncoids (Figure 10j and Figure S5), lending support for a similar origin for the tubule microstructures. In contrast, measurements of minimum tubule diameters for known spiculate sponges with a 'sponge mummy' morphology and rectilinear sparitic microstructures reported in Neuweiler et al., 2023 show a statistically significant difference ($p<0.0001$) to tubule diameter values in the CM microbialites (Figure S6 and Table S3). The combination of (1) a sponge mummy mesostructure with (2) a distinct rectilinear sparitic microfabric, and (3) larger tubule diameters than those typically reported for vermiform microstructure, highlight important differences between accepted 'sponge mummies' (Neuweiler et al., 2023) and the observations presented herein for Recent oncoids, the CM microbialites, and unlithified biofilm channels.

In the CM microbialites, it is unlikely that the microbialites experienced subaerial exposure that resulted in open cavities (Figure 9c') as in the Recent oncoid grains, but rather the microsparitic tubules were likely lithified nearly synchronously with the lithification of the biofilm under anomalously high carbonate supersaturation. Evidence for early lithification is demonstrated by the fully cemented vermiform network and surrounding micrite in what we interpret to be a microbial detachment structure (see Figure 10 in Stewart, 2012) that was sufficiently cemented *in situ* at the seafloor to maintain rigidity and preserve its microsparitic network together with its micritic rounded border and internal circular cross section of the larger-scale (~150 microns) microbial branching (Figures 5e-f). The syngenetic precipitation of crystals

415 in the biomass surrounding the tubular water channels is required for preservation of the two
416 textures (micrite and microspar) in the CM microbialites. Studies have shown that EPS solutions
417 produce smaller and more abundant $CaCO_3$ crystals compared to EPS-poor regions (Martinho De
418 Brito *et al.*, 2023), providing experimental context for the change in grain size from micrite to
419 progressively more sparitic in the direction of a tubule or a pore. This taphonomic model of early
420 cementation associated with carbonates that form in waters with anomalously high carbonate
421 supersaturation or under evaporative conditions that lithify at or near the sediment water
422 interface before compaction is well-recognized in the creation of fenestral fabrics (Choquette &
423 Pray, 1970).

424 Fenestra are defined as spaces that have no apparent support in the framework of primary
425 grains composing the sediment (Tebbutt *et al.*, 1965), as is typical of vermiform microstructure.
426 We consequently regard vermiform microstructure as a type of fenestral fabric (*sensu* Tebbutt *et*
427 *al*., 1965) representing a cement-filled primary void that is fabric selective. The highly variable
428 vermiform geometries observed in the CM microbialites suggest that (1) there are likely intrinsic
429 (e.g., microbial community composition) and extrinsic (e.g., environmental) controls on the
430 creation of tubule geometries, (2) tubule preservation is largely dependent on the rates of
431 calcification and (3) not all features represent water channels *sensu stricto*, but rather could
432 simply represent EPS-poor or microbial-poor regions of the biofilm structure. While vermiform
433 microstructure has been possibly attributed to fenestral fabrics (Neuweiler *et al*., 2023), the
434 distinct, principal hypothesis of this study is the attribution of the tubular anastomosing
435 geometries of variable morphologies that exhibit nearly uniform diameters (Figure 1) to biofilm
436 channels described in modern experiments. The extreme diameter uniformity in tubule 3D
437 architecture with distinct circular cross-sections that typify some of the diagnostic examples of

438 vermiform microstructure from the rock record (e.g., Park *et al*., 2015), likely represent an end-
439 member of tubule morphology that is preserved under unique geochemical conditions.
440 Deviations from diameter uniformity and 3D branching, likely represent biofilm pores or other
441 microbial-poor regions of a biofilm.

442 The biofilm channel hypothesis for vermiform microstructure is further supported by
443 additional observations in the CM microbialites. For example, the basal laminated layer of the
444 CM contains evidence of restriction in the form of calcite pseudomorphs after gypsum (Ibarra *et*
445 *al.*, 2014), indicating evidence of hypersalinity. The occurrence of vermiform microstructure
446 from shallow environments suggests the vermiform fabric could be a response to limited nutrient
447 availability or a response to shallow water conditions. Biofilm channel formation increases
448 permeability within hydrated biofilms (Costerton *et al.,*1994), suggesting that microtubule
449 formation may represent a structural response for a need to increase water flow to the internal
450 regions of a living biofilm, giving the tubules a similar function to the vascular system of plants
451 and animals (Penesyan *et al.*, 2021). In turn, the delivery of seawater and solutes enhances the
452 preservation potential of the channel's (tubule) morphology via delivery of carbonate ions that
453 precipitate synsedimentary cements within them.

454 A remaining limitation in comparing non lithified biofilms to microbialite rock textures is
455 the uncertainty surrounding the effects of lithification on biofilm structural integrity. While
456 biofilms can create 3D tubule networks (Figure 8), lithification of the biofilm must happen early
457 enough (before burial) for the preservation of delicate tubule structures. Calcite precipitation
458 within hollow tubule networks (e.g., Figure 9d) has yet to be demonstrated in a laboratory or
459 natural setting, making it difficult to evaluate the extent to which pore occluding cements may
460 alter tubule morphology.

6 GEOLOGIC SIGNIFICANCE

Nearly all reported examples of vermiform microstructure attributed to keratose sponges occur within or are associated with microbialites–structures composed of lithified biofilms (Burne & Moore, 1987)–thus lending support for a biofilm channel origin for vermiform microstructure. The biofilm channel hypothesis for the creation of vermiform microstructure based on experimental data can help explain several of its enigmatic features including its (1) taphonomy, (2) temporal distribution, and (3) range of tubule diameters observed.

(1) The uniform taphonomic mode of preservation for vermiform fabric (i.e., microsparitic tubules in a matrix of micrite) likely results from the cementation of open biofilm channels (tubules) after lithification of the EPS portion of the biofilm, which is a similar process to the precipitation of synsedimentary cements that fill fenestral textures (Figures 2d-e). Similarly delicate metabolic gas bubbles within biofilms have been shown to leave a morphologic record in ancient stromatolites and are often preserved as microspar-filled fenestrae (Bosak *et al.*, 2009). While bubble formation is a distinct process from the hypothesized creation of tubular channels described herein, bubbles are also seemingly delicate structures that are preserved nonetheless under the right geochemical conditions. It is likely that water-filled anastomosing channels observed in modern biofilms can preserve a morphologic record of tubular geometries if the microbial community develops in aquatic environments with anomalously high supersaturation with respect to calcium carbonate to promote rapid lithification.

(2) Accordingly, there is a preponderance of vermiform microstructure reports in microbialites that formed during times of anomalously high seawater carbonate saturation. These time periods include, but are not limited to, the Neoproterozoic (Turner, 2021), the Cambro-

Ordovician (Lee and Riding, 2021), Cambrian (Lee *et al*., 2014), Triassic (Pei *et al.*, 2021; Wu *et al.*, 2022), and during the aftermath of the end-Permian (Heindel *et al.*, 2018; Baud *et al.*, 2021), providing a temporal and geochemical mechanism for the preservation of delicate biofilm microstructures. Many of the examples listed also occur adjacent to and in the interstices of calcium carbonate crystal fans (Friesenbichler *et al.*, 2018; Baud *et al.*, 2021), which represent hallmarks of anomalously high carbonate supersaturation (Grotzinger & Knoll, 1995; Woods *et al.*, 1999). Thus far, channel networks and lithified biofilm microstructures have been attributed to micritic veneers lining carbonates from cryptic habitats (Riding, 2002), and here we suggest that lithified biofilm channel networks may be more common than previously considered.

(3) The interpretation of vermiform fabric as biofilm channels also addresses the range of microtubule sizes observed for vermiform geometries from the same rock unit or within a single microbialite unit (Luo and Reitner, 2016; Friesenbichler *et al.*, 2018). Modern microbial mats exhibit network fabrics that occur at many scales resulting in fractal-like morphologies (Kropp *et al.*, 1997). Similar larger geometries of 3D microstructures can be found in modern microbial mats (Shepard & Sumner, 2010; Sim *et al.*, 2012), resulting from microbial mat growth in systems limited by diffusion (Petroff *et al.*, 2010). In the CM microbialites, we observe at least two microstructural scales of fenestra development associated with the dendrolitic layers (inter and intra-dendrolite spacing labeled in Figure 3). Many of the dendrolite structures also exhibit classic mushroom shapes in vertical cross-section (Figures 4c-d and Figure 7b), which represent the observed and modeled architecture of a mature biofilm macrocolony (Flemming and Wingender, 2010). Recent interpretations of larger round morphologies associated with vermiform microstructure have been attributed to sponge canals (Lee & Riding, 2022; Luo *et al.*, 2022), but can be more parsimoniously explained by a larger scale of biofilm fenestrae,

507 demonstrated in the CM as inter-dendrolite spacing (Figure 3). The shape and size of the larger
508 tubular features would help explain the range of vermiform diameters seen in microbialite
509 deposits (Luo & Reitner, 2014, 2016; Lee & Riding, 2022). Similar fractal-like fenestral patterns
510 are common in other ancient microbialites such as Ordovician stromatolitic reefs (Figures 11a-
511 b), the Neoproterozoic Noonday Dolomite (Fraiser & Corsetti, 2003) (Figures 11c-d), as well as
512 in modern dendrolitic cones in hot spring settings (Bradley *et al.*, 2017).

513 The similarity in shape, size, and distribution of microspar-filled tubules in a micritic
514 matrix within a microbialite unit shared with channel geometries in extant microbial biofilms
515 indicates the vermiform microstructure can be created in the absence of sponges. Microbial
516 communities produce 3D channel networks that could potentially be preserved in the geologic
517 record as anastomosing tubular microstructures. If the biofilm channel hypothesis for vermiform
518 microstructure is correct, it would allow for a unique understanding of mature 3D biofilm
519 architecture that extends to at least the Neoproterozoic (Turner, 2021) which is often difficult to
520 resolve in modern biofilm analyses (Yan *et al.*, 2016). As sampling and imaging techniques on
521 living natural aquatic biofilms improve, modern observations will help reveal the significance of
522 the variable vermiform geometries observed in the rock record. We do not suggest that all reports
523 of sponge body fossils that contain a tubular texture represent microbial features. For example,
524 exceptionally preserved chitin in a sponge fossil from the Burgess Shale preserves features
525 attributed to a keratosan sponge that scales with the shape of the skeletal sponge body fossil
526 (Walcott, 1920; Ehrlich *et al.*, 2013). Instead, our analyses provide sufficient evidence for a need
527 to reevaluate the keratose sponge interpretation for vermiform microstructure in carbonate
528 microbialites and in turn may reveal a new opportunity to explore the significance of biofilm
529 channel networks at different scales of biofilm development in ancient carbonates.

7 CONCLUSION

We describe a wide array of vermiform geometries in the Upper Triassic Cotham Marble microbialites. The vermiform geometries are comparable and nearly identical to many examples of vermiform geometries from Phanerozoic and Neoproterozoic microbialites that have been interpreted as keratose sponge body fossils. Observations of microfossil distribution, lateral continuity, and flat-pebble facies, are all evidence against the presence of sponges in the CM microbialites. Comparison of modern biofilm channels with vermiform geometries in the CM microbialites and Recent freshwater oncoids suggest a similar origin. We hypothesize the vermiform microstructure is a morphologic record of cemented intra-biofilm water channels in ancient microbial deposits that grew in seawater with anomalously high carbonate supersaturation.

REFERENCES

Anderson RP, Woltz CR, Tosca NJ, Porter SM, Briggs DEG (2023) Fossilisation processes and our reading of animal antiquity. *Trends in Ecology and Evolution* **38**, 1060–1071.

Antcliffe JB, Callow RHT, Brasier MD (2014) Giving the early fossil record of sponges a squeeze. *Biological Reviews* **89**, 972–1004.

Baud A, Richoz S, Brandner R, Krystyn L, Heindel K, Mohtat T, Mohtat-Aghai P, Horacek M (2021) Sponge Takeover from End-Permian Mass Extinction to Early Induan Time: Records in Central Iran Microbial Buildups. *Frontiers in Earth Science* **9**, 1–23.

Beer D de, Stoodley P, Roe F, Lewandowski Z (1994) Effects of biofilm structures on oxygen distribution and mass transport. *Biotechnology and Bioengineering* **43**, 1131–1138.

Bosak T, Liang B, Min SS, Petroff AP (2009) Morphological record of oxygenic photosynthesis in conical stromatolites. *Proceedings of the National Academy of Sciences of the United*

553 *States of America* **106**, 10939–10943.
554 Botting JP (2005) Exceptionally well-preserved middle Ordovician sponges from the Llandegley
555 rocks lagerstätte, Wales. *Palaeontology* **48**, 577–617.
556 Bottura B, Rooney LM, Hoskisson PA, McConnell G (2022) Intra-colony channel morphology
557 in Escherichia coli biofilms is governed by nutrient availability and substrate stiffness.
558 *Biofilm* **4**, 1–14.
559 Brachert TC, Dullo W-C, Stoffers P (1987) Diagenesis of Siliceous Sponge Limestones from the
560 Pleistocene of the Tyrrhenian Sea (Mediterranean Sea). *Facies* **17**, 41–49.
561 Bradley JA, Daille LK, Trivedi CB, Bojanowski CL, Stamps BW, Stevenson BS, Nunn HS,
562 Johnson HA, Loyd SJ, Berelson WM, Corsetti FA, Spear JR (2017) Carbonate-rich
563 dendrolitic cones: Insights into a modern analog for incipient microbialite formation, Little
564 Hot Creek, Long Valley Caldera, California. *npj Biofilms and Microbiomes* **3**.
565 Brasier MD, Antcliffe JB, Callow RHT (2011) Evolutionary Trends in Remarkable Fossil
566 Preservation Across the Ediacaran-Cambrian Transition and the Impact of Metazoan
567 Mixing. In: *Taphonomy: Process and Bias Through Time* (eds. Allison PA, Bottjer DJ).
568 Springer, Netherlands.
569 Burne R V., Moore LS (1987) Microbialites: Organosedimentary Deposits of Benthic Microbial
570 Communities. *Palaios* **2**, 241.
571 Choquette P, Pray L (1970) Geologic Nomenclature and Classification of Porosity in
572 Sedimentary Carbonates. *American Association of Petroleum Geologists Bulletin* **54**, 207–
573 250.
574 Corsetti FA, Grotzinger JP (2005) Origin and significance of tube structures in Neoproterozoic
575 post-glacial cap carbonates: Example from Noonday Dolomite, Death Valley, United States.

576 *Palaios* **20**, 348–362.
577 Costerton JW, Lewandowski Z, DeBeer D, Caldwell D, Korber D, James G (1994) Biofilms, the
578 customized microniche. *Journal of Bacteriology* **176**, 2137–2142.
579 Decho AW, Visscher PT, Reid RP (2005) Production and cycling of natural microbial
580 exopolymers (EPS) within a marine stromatolite. *Palaeogeography, Palaeoclimatology,*
581 *Palaeoecology* **219**, 71–86.
582 Dupraz C, Fowler A, Tobias C, Visscher PT (2013) Stromatolitic knobs in Storr's Lake (San
583 Salvador, Bahamas): A model system for formation and alteration of laminae. *Geobiology*
584 **11**, 527–548.
585 Dupraz C, Visscher PT (2005) Microbial lithification in marine stromatolites and hypersaline
586 mats. *Trends in Microbiology* **13**, 429–438.
587 Ehrlich H, Rigby JK, Botting JP, Tsurkan M V., Werner C, Schwille P, Petrášek Z, Pisera A,
588 Simon P, Sivkov VN, Vyalikh D V., Molodtsov SL, Kurek D, Kammer M, Hunoldt S, Born
589 R, Stawski D, Steinhof A, Bazhenov V V., Geisler T (2013) Discovery of 505-million-year
590 old chitin in the basal demosponge Vauxia gracilenta. *Scientific Reports* **3**, 17–20.
591 Flemming HC, Wingender J (2010) The biofilm matrix. *Nature Reviews Microbiology* **8**, 623–
592 633.
593 Flügel E (2004) *Microfacies of Carbonate Rocks: Analysis, Interpretation, and Application*.
594 Springer, New York.
595 Fraiser ML, Corsetti FA (2003) Neoproterozoic Carbonate Shrubs : Interplay of Microbial
596 Activity and Unusual Environmental Conditions in Post-Snowball Earth Oceans **18**, 378–
597 387.
598 Friesenbichler E, Richoz S, Baud A, Krystyn L, Sahakyan L, Vardanyan S, Peckmann J, Reitner

599 J, Heindel K (2018) Sponge-microbial build-ups from the lowermost Triassic Chanakhchi
600 section in southern Armenia: Microfacies and stable carbon isotopes. *Palaeogeography,*
601 *Palaeoclimatology, Palaeoecology* **490**, 653–672.
602 Froget C (1976) Observations sur l'altération de la silice et des silicates au cours de la
603 lithification carbonatée (Région Siculo-Tunisienne). *Géologie Méditerranéenne* **3**, 219–225.
604 Geisel S, Secchi E, Vermant J (2022) The role of surface adhesion on the macroscopic wrinkling
605 of biofilms. *eLife* **11**, 1–19.
606 Grey K, Awramik SM (2020) *Handbook for the study and description of microbialites*.
607 *Geological Survey of Western Australia Bulletin 147*.
608 Grotzinger JP, Knoll AH (1995) Anomalous carbonate precipitates: is the Precambrian the key to
609 the Permian? *Palaios* **10**, 578–596.
610 Gürich GJE (1906) *Les spongiostromides du viséen de la province de Namur*. *Mémoires du*
611 *Musée royal d'histoire naturelle de Belgique = Verhandelingen van het Koninklijk*
612 *Natuurhistorisch Museum van Belgie*. Imprimerie Polleunis & Ceuterick.
613 Hamilton D (1961) Algal growths in the Rhaetic Cotham marble of southern England.
614 *Palaeontology* **4**, 324–333.
615 Heindel K, Foster WJ, Richoz S, Birgel D, Roden VJ, Baud A, Brandner R, Krystyn L, Mohtat
616 T, Koşun E, Twitchett RJ, Reitner J, Peckmann J (2018) The formation of microbial-
617 metazoan bioherms and biostromes following the latest Permian mass extinction. *Gondwana*
618 *Research* **61**, 187–202.
619 Hesselbo SP, Robinson SA, Surlyk F (2004) Sea-level change and facies development across
620 potential Triassic–Jurassic boundary horizons, SW Britain. *Journal of the Geological*
621 *Society* **161**, 365–379.

622 Hopkins MJ, Gerber S (2020) Evolutionary Developmental Biology. *Evolutionary*
623 *Developmental Biology*.
624 Ibarra Y, Corsetti FA (2016) Lateral comparative investigation of stromatolites: Astrobiological
625 implications and assessment of scales of control. *Astrobiology* **16**, 271–281.
626 Ibarra Y, Corsetti FA, Greene SE, Bottjer DJ (2014) Microfacies of the Cotham Marble: A
627 tubestone carbonate microbialite from the Upper Triassic Southwestern U.K. *Palaios* **29**, 1–
628 15.
629 Ibarra Y, Corsetti FA, Greene SE, Bottjer DJ (2015) Microfacies of the Cotham Marble: A
630 tubestone carbonate microbialite from the Upper Triassic Southwestern U.K.: A Reply.
631 *Palaios* **30**, 806–809.
632 Ibarra Y, Corsetti FA, Greene SE, Bottjer DJ (2016) A microbial carbonate response in
633 synchrony with the end-Triassic mass extinction across the SW UK. *Scientific Reports* **6**.
634 Jesionowski T, Norman M, Zółtowska-Aksamitowska S, Petrenko I, Joseph Y, Ehrlich H (2018)
635 Marine spongin: Naturally prefabricated 3D scaffold-based biomaterial. *Marine Drugs* **16**,
636 1–23.
637 Kershaw S, Li Q, Li Y (2021) Addressing a Phanerozoic carbonate facies conundrum—sponges
638 or clotted micrite? Evidence from Early Silurian reefs, South China Block. *The Sedimentary*
639 *Record* **19**, 3–10.
640 Kropp J, Block A, Bloh W Von, Klenke T, Schellnhuber HJ (1997) Multifractal characterization
641 of microbially induced magnesian calcite formation in recent tidal flat sediments.
642 *Sedimentary Geology* **109**, 37–51.
643 Lawrence JR, Korber DR, Hoyle BD, Costerton JW, Caldwell DE (1991) Optical sectioning of
644 microbial biofilms. *Journal of Bacteriology* **173**, 6558–6567.

645 Lee J-H, Riding R (2022) Recognizing sponge in Spongiostroma Gürich, 1906 from the
646 Mississippian of Belgium . *Journal of Paleontology* 1–12.
647 Lee JH, Chen J, Choh SJ, Lee DJ, Han Z, Chough SK (2014) Furongian (late Cambrian) sponge-
648 microbial maze-like reefs in the north China platform. *Palaios* **29**, 27–37.
649 Lee JH, Riding R (2021) The 'classic stromatolite' Cryptozoön is a keratose sponge-microbial
650 consortium. *Geobiology* **19**, 189–198.
651 Lei W, Krolla P, Schwartz T, Levkin PA (2020) Controlling Geometry and Flow Through
652 Bacterial Bridges on Patterned Lubricant-Infused Surfaces (pLIS). *Small* **16**, 1–7.
653 Luo C, Pei Y, Richoz S, Li Q, Reitner J (2022) Identification and Current Palaeobiological
654 Understanding of "Keratosa"-Type Nonspicular Demosponge Fossils in Carbonates: With a
655 New Example from the Lowermost Triassic, Armenia. *Life* **12**.
656 Luo C, Reitner J (2014) First report of fossil "keratose" demosponges in Phanerozoic carbonates:
657 Preservation and 3-D reconstruction. *Naturwissenschaften* **101**, 467–477.
658 Mackey TJ, Sumner DY, Hawes I, Jungblut AD, Lawrence J, Leidman S, Allen B (2017)
659 Increased mud deposition reduces stromatolite complexity. *Geology* **45**, 663–666.
660 Marenco PJ, Corsetti FA, Bottjer DJ (2002) Noonday Tubes: Observations and reinterpretations
661 based on better preservation from a new locality. In: *Proterozoic-Cambrian of the Great*
662 *Basin and Beyond, Pacific Section Book 93* (ed. Cooper J). Pacific Section, SEPM (Society
663 for Sedimentary Geology), pp. 31–35.
664 Martinho De Brito M, Bundeleva I, Marin F, Vennin E, Wilmotte A, Plasseraud L, Visscher PT
665 (2023) Properties of exopolymeric substances (EPSs) produced during cyanobacterial
666 growth: potential role in whiting events. *Biogeosciences* **20**, 3165–3183.
667 Mehra A, Watters WA, Grotzinger JP, Maloof AC (2020) Three-dimensional reconstructions of

668 the putative metazoan Namapoikia show that it was a microbial construction. *Proceedings*
669 *of the National Academy of Sciences of the United States of America* **117**, 19760–19766.
670 Neuweiler F, Kershaw S, Boulvain F, Matysik M, Sendino C, McMenamin M, Munnecke A
671 (2023) Keratose sponges in ancient carbonates – A problem of interpretation. *Sedimentology*
672 **70**, 927–968.
673 Otsu N, Smith PL, Reid DB, Environment C, Palo L, Alto P, Smith PL (1979) A Threshold
674 Selection Method from Gray-Level Histograms. *IEEE Transactions on Systems, Man, and*
675 *Cybernetics* **C**, 62–66.
676 Park J, Lee JH, Hong J, Choh SJ, Lee DC, Lee DJ (2015) An Upper Ordovician sponge-bearing
677 micritic limestone and implication for early Palaeozoic carbonate successions. *Sedimentary*
678 *Geology* **319**, 124–133.
679 Pei Y, Duda JP, Schönig J, Luo C, Reitner J (2021) Late Anisian microbe-metazoan build-ups in
680 the Germanic Basin: aftermath of the Permian–Triassic crisis. *Lethaia* **54**, 823–844.
681 Penesyan A, Paulsen IT, Kjelleberg S, Gillings MR (2021) Three faces of biofilms: a microbial
682 lifestyle, a nascent multicellular organism, and an incubator for diversity. *npj Biofilms and*
683 *Microbiomes* **7**, 1–9.
684 Petroff AP, Sim MS, Maslov A, Krupenin M, Rothman DH, Bosak T (2010) Biophysical basis
685 for the geometry of conical stromatolites. *Proceedings of the National Academy of Sciences*
686 *of the United States of America* **107**, 9956–9961.
687 Petryshyn VA, Greene SE, Farnsworth A, Lunt DJ, Kelley A, Gammariello R, Ibarra Y, Bottjer
688 DJ, Tripati A, Corsetti FA (2020) The role of temperature in the initiation of the end-
689 Triassic mass extinction. *Earth-Science Reviews* **208**, 103266.
690 Pratt BR (1982) Stromatolitic framework of carbonate mud-mounds. *Journal of Sedimentary*

691 *Petrology* **52**, 1203–1227.
692 Quan K, Hou J, Zhang Z, Ren Y, Peterson BW, Flemming HC, Mayer C, Busscher HJ, Mei HC
693 van der (2022) Water in bacterial biofilms: pores and channels, storage and transport
694 functions. *Critical Reviews in Microbiology* **48**, 283–302.
695 Riding R (2002) Biofilm architecture of Phanerozoic cryptic carbonate marine veneers. *Geology*
696 **30**, 31–34.
697 Ritterbush KA, Rosas S, Corsetti FA, Bottjer DJ, West AJ (2015) Andean sponges reveal long-
698 term benthic ecosystem shifts following the end-Triassic mass extinction. *Palaeogeography,*
699 *Palaeoclimatology, Palaeoecology* **420**, 193–209.
700 Rooney LM, Amos WB, Hoskisson PA, McConnell G (2020) Intra-colony channels in E. coli
701 function as a nutrient uptake system. *ISME Journal* **14**, 2461–2473.
702 Sepkoski JJ (1982) Flat-Pebble Conglomerates, Storm Deposits, and the Cambrian Bottom
703 Fauna. In: *Cyclic and Event Stratification* (eds. Einsele G, Seilacher A). Springer Berlin
704 Heidelberg, Berlin, Heidelberg, pp. 371–385.
705 Shapiro RS (2000) A Comment on the Systematic Confusion of Thrombolites. *Palaios* **15**, 166.
706 Shepard RN, Sumner DY (2010) Undirected motility of filamentous cyanobacteria produces
707 reticulate mats. *Geobiology* **8**, 179–190.
708 Sim MS, Liang B, Petroff AP, Evans A, Klepac-Ceraj V, Flannery DT, Walter MR, Bosak T
709 (2012) Oxygen-dependent morphogenesis of modern clumped photosynthetic mats and
710 implications for the archean stromatolite record. *Geosciences (Switzerland)* **2**, 235–259.
711 Stewart PS (2012) Mini-review: Convection around biofilms. *Biofouling* **28**, 187–198.
712 Stocchino GA, Cubeddu T, Pronzato R, Sanna MA, Manconi R (2021) Sponges architecture by
713 colour: new insights into the fibres morphogenesis, skeletal spatial layout and morpho-

anatomical traits of a marine horny sponge species (Porifera). *European Zoological Journal* **88**, 237–253.

Stoodley P, DeBeer D, Lewandowski Z (1994) Liquid flow in biofilm systems. *Applied and Environmental Microbiology* **60**, 2711–2716.

Taylor MW, Radax R, Steger D, Wagner M (2007) Sponge-Associated Microorganisms: Evolution, Ecology, and Biotechnological Potential. *Microbiology and Molecular Biology Reviews* **71**, 295–347.

Tebbutt GE, Conley CD, Boyd DW (1965) Lithogenesis of a distinctive carbonate rock fabric. *University of Wyoming Contributions to Geology* **4**, 1–13.

Turner EC (2021) Possible poriferan body fossils in early Neoproterozoic microbial reefs. *Nature* **596**, 87–91.

Walcott CD (1920) Cambrian geology and paleontology. IV. Middle Cambrian Spongiae. *Smithsonian Miscellaneous Collections* **67**, 261–364.

Walter MR (1972) Stromatolites and the Biostratigraphy of the Australian Pre- cambrian and Cambrian. *The Palaeontological Association of London, Special Papers in Palaeontology* **11**, 256.

Wilking JN, Zaburdaev V, Volder M De, Losick R, Brenner MP, Weitz DA (2013) Liquid transport facilitated by channels in Bacillus subtilis biofilms. *Proceedings of the National Academy of Sciences of the United States of America* **110**, 848–852.

Woods AD, Bottjer DJ, Mutti M, Morrison J (1999) Lower Triassic large sea-floor carbonate cements: Their origin and a mechanism for the prolonged biotic recovery from the end-Permian mass extinction. *Geology* **27**, 645–648.

Wright VP, Mayall M (1981) Organism-Sediment Interactions in Stromatolites: an Example

from the Upper Triassic of South West Britain. *Phanerozoic Stromatolites* 74–84.

Wu S, Chen ZQ, Su C, Fang Y, Yang H (2022) Keratose sponge fabrics from the lowermost Triassic microbialites in South China: Geobiologic features and Phanerozoic evolution. *Global and Planetary Change* **211**, 103787.

Yan J, Sharo AG, Stone HA, Wingreen NS, Bassler BL (2016) Vibrio cholerae biofilm growth program and architecture revealed by single-cell live imaging. *Proceedings of the National Academy of Sciences of the United States of America* **113**, e5337–e5343.

Zhang N, Thompson CEL, Townend IH, Rankin KE, Paterson DM, Manning AJ (2018) Nondestructive 3D Imaging and Quantification of Hydrated Biofilm-Sediment Aggregates Using X-ray Microcomputed Tomography. *Environmental Science and Technology* **52**, 13306–13313.

FIGURE CAPTIONS

FIGURE 1. Comparison of vermiform microstructure from the rock record to microstructures in the Cotham Marble microbialites. (a) *Madiganites mawsoni* from Walter (1972) considered a type of vermiform laminar architecture (Grey & Awramik, 2020). (b) Bifurcating, microsparry, tubular geometries from the basal laminated layer (L1 in Ibarra et al., 2014) of the Cotham Marble microbialites. (c) Close-up of microspar-cemented microtubular fabric in a micritic matrix from the Cotham Marble. (d-e) Tubular microstructure from the basal laminated layer (L1) in samples from Bristol. (f) Vermiform geometries in Cambrian *Cryptozoon* stromatolites (Lee and Riding, 2021b); note resemblance in size as well as microstructure texture and fabric to (d). (g) Vermiform geometries in Upper Cambrian maze-like reefs interpreted as a sponge ('S') texture (Lee et al., 2014); note resemblance in size and tubule microstructure texture and fabric to (e). (h-i) Microtubular structures in the dendrolitic phases of the Cotham Marble from Bristol

760 (h) and Stowey Quarry (i) that occur in the interdendrolite region (h), and within the dendrolites
761 (i). (j) Vermiform microstructure in Upper Ordovician micritic limestones (Park et al., 2015)
762 with arrow denoting similar branching morphologies to arrow in (h). (k) Vermiform
763 microstructure from Neoproterozoic reefs (Turner, 2021); compare to microstructure fabric,
764 texture and size in (i) with tubules denoted with arrows.
765 FIGURE 2. Comparison of sparry microtubular geometries in the Cotham Marble microbialites
766 to adjacent synsedimentary cements. (a) Thin-section, high-resolution scan of the laminated layer
767 L1 from Bristol. (b) Micritic tuft and associated laminoid fenestra. (c) Vermiform
768 microstructure. (d) Laminoid fenestra. (e) Fenestra associated with the tops of micritic tufted
769 cones. (f) Close-up of vermiform microstructure in (c). (g) Detail of vermiform microstructure.
770 Note the similarity in calcite cement fill between (d), (e), and (g) suggesting all were once open
771 cavities that fill with synsedimentary cement.
772 FIGURE 3. Polished high-resolution scans denoting two scales of tubular geometries in the
773 dendrolitic layers of the Cotham Marble microbialites. (a) Vertically-oriented dendrolitic
774 mesostructure (cm-scale) denoting the dendrolites “d” and inter-dendrolite regions “f”. (b)
775 Horizontal cross-section of a polished sample through the dendrolitic region denoting the inter-
776 dendrolite spacing of uniform diameter with arrows. (c-d) Oblique cross-section of the
777 dendrolites revealing inter-dendrolite regions with tubular branching and circular cross-sections.
778 (e-h) Mesostructure to microstructure detail of microtubular geometries labeled ‘intra-dendrolite
779 fenestra’ present within the dendrolites (arrows in f and h). Samples a-d are from Manor Farm
780 and samples e-h are from Bristol.
781 FIGURE 4. Thin-section photomicrographs of intra-dendrolite vermiform microstructure in a
782 sample from Stowey Quarry. (a) Submillimeter-scale branching morphology of a dendrolite. (b)

Vermiform microstructures within the dendrolitic fabric are the bright, microsparitic tubular structures and the opaque dark features in the dark micritic regions are pyrite-coated possible microfossils (Ibarra et al., 2014). (c) Dendrolitic micritic protrusions that contain vermiform microstructure (vm) with anastomosing tubules of uniform diameter (d) higher resolution image of (c). (e-f) Vermiform geometries displaying somewhat of a 3D stitch pattern with distinct circular cross-sections (arrows) in a micritic matrix that are restricted to the dendrolitic regions. (g) Histogram of minimum tubule diameters (in microns) measured for facies L1 and D1 of the CM microbialites and inter-dendrolite fenestra of CM microbialites (Appendix S1).

FIGURE 5. Examples of rare vermiform microstructure (vm) in the inter-dendrolite fill in samples from Bristol (a-d) and Manor Farm (e-f). (a) Thin-section photomosaic of dendrolite phase D1 overlain by micritic laminae above. (b-d) Detail of (a) denoting with arrows the inter-dendrolite micrite and its associated vm; note the presence of a 'bridge' structure (*sensu* Marenco *et al.*, 2002; Corsetti and Grotzinger, 2005) connecting adjacent dendrolite 'branches' and clear circular tubule cross-sections denoted with arrows in the lower part of (d). (e-f) A detached dendrolite 'branch' deposited in the inter-dendrolite fill; the arrows in (f) denote a sharp boundary with the surrounding matrix and the arrows inside the dendrolite point to a larger-scale rounded morphology.

FIGURE 6. Fine-scale lateral continuity of vermiform geometries across microbialite samples from three locations (a) Bristol, (b) Manor Farm Quarry, (c) Stowey Quarry, representing a minimum distance of at least ~20 km between sample sites (Ibarra et al., 2014; Ibarra and Corsetti, 2016). All photomicrographs were taken using a white card; vm=vermiform microstructure, d=dendrolite.

FIGURE 7. Flat-pebble conglomerate facies. (a) Polished high-resolution scan of flat-pebble “p” conglomerate facies from the Bristol Museum and Art Gallery (labeled ‘Crazy’ Cotham Marble, Specimen number CB 4144 B), arrows denote mm-scale micritic protrusions around the flat-pebble clasts. (b-c) Thin section photomicrograph cross-section of a flat pebble “p” from Lower Woods showing millimeter-scale micritic protrusions, the arrows in (c) denote a larger-scale tubule structure similar to those in Figures 4b-d. (d-e) Photomicrographs denoting detail in (b) that contain anastomosing, microsparitic tubular geometries separated by micritic regions. (f-g) Detail from (b) and (c) denoting with arrows the variable geometric patterns within the micritic protrusions.

FIGURE 8. Comparison of vermiform geometries to examples from modern biofilm channels. (a-c) Examples of tubular microstructure from the CM demonstrating similar morphologies to modern biofilm water channels (a') Wilking et al., 2013, (b') (Geisel *et al.*, 2022), and (c') Wilking et al., 2013. Channel morphologies in (a') and (c') are highlighted with an aqueous fluorescent green dye imaged using confocal microscopy. (b') is a phase contrast image of a *Pseudomonas aeruginosa* biofilm where the development of hollow channels (pictured) are shown to increase the effective volume occupied by the biofilm (Geisel *et al.*, 2022). (d-f) Pore water (d), biofilm (e), and (f) biofilm superimposed 2D relationships between the pore water and biofilm of a partitioned 3D biofilm sediment aggregate from Zhang et al., 2018. Note the tubular, branching geometries and circular cross-sections of the pore water. (g) Interpretation of sparitic and micritic regions of the Cotham Marble as lithified water channels and biofilm.

FIGURE 9. A conceptual model of vermiform microstructure paragenesis. (a) Mesostructure of a living aquatic biofilm. (b) Detail of (a) where laminar and/or dendrolitic biofilms are composed of an EPS-enclosed microbial community with hydrated EPS-poor regions and anastomosing

828 water channels. (b) EPS-rich regions of the biofilm are preferentially lithified by a micrite-
829 precipitating microbial community leaving water-filled, tubular interstices between the lithified
830 micritic regions. (c') If the partially-lithified biofilm is subaerially exposed, tubular pore space
831 can result. (d) Microsparitic, pore-occluding cements fill the tubular interstices, creating a grain
832 size contrast between the microsparitic tubules and the EPS-associated micrite. (e) Resulting
833 vermiform microstructure.
834 FIGURE 10. Vermiform geometries in modern, spring-associated, freshwater coated grains from
835 the Spring Mountains, Nevada. (a) Coated-grains in an *in situ* position accrete along the creek.
836 (b) High-resolution scan of a slabbed coated grain showing a well-laminated mesostructure. (c)
837 Thin section photomicrograph of a laminar microstructure containing dense micritic bands that
838 alternate with porous bands. (d-e) Detail of (c) showing a somewhat tubular open pore network
839 in a micritic matrix. (f-i) Network of hollow tubules aligned along laminar bands resembling
840 vermiform geometries. (j) Violin plot showing similarity of tubular pore diameters in freshwater
841 oncoids to L1 and D1 vermiform microstructure tubule diameters in CM microbialites.
842 PPL=plane polarized light, XPL= cross-polarized light.
843 FIGURE 11. Larger-scale fenestral patterns in microbialites from the rock record. (a)
844 Stromatolitic reefs from the Ordovician denoting larger-scale fenestral pattens in a thin-section
845 photomicrograph (b). (c) Noonday Dolomite photomicrograph of micritic shrub facies (c) and
846 outcrop photo (d) from (Fraiser & Corsetti, 2003) with comparison to larger-scale fenestral
847 patterns to (b).

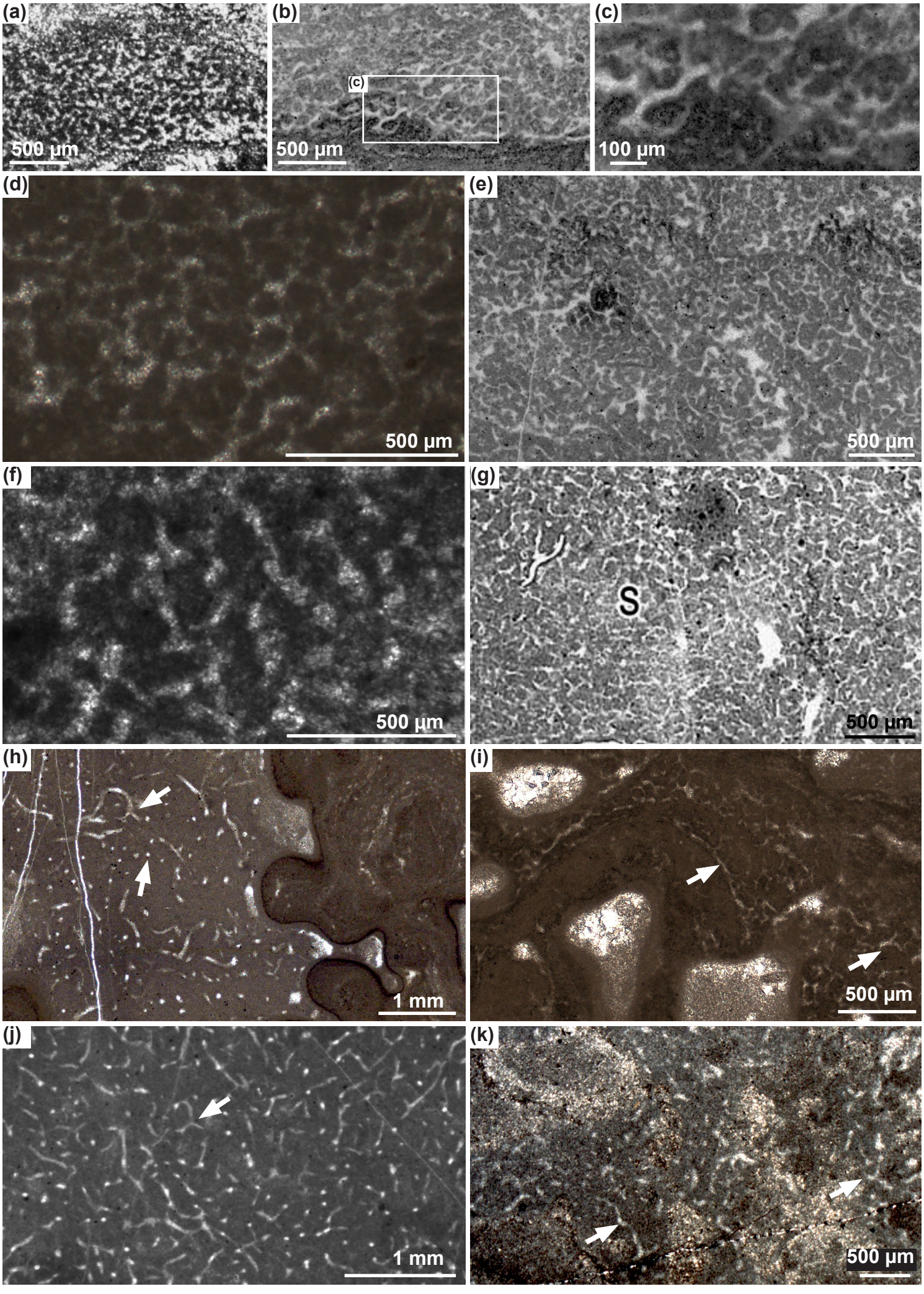
(a)
500 µm
(b)
(c)
500 µm
(c)
100 µm
(d)
500 µm
(e)
500 µm
(f)
500 µm
(g)
S
500 µm
(h)
1 mm
(i)
500 µm
(j)
1 mm
(k)
500 µm

Figure 2

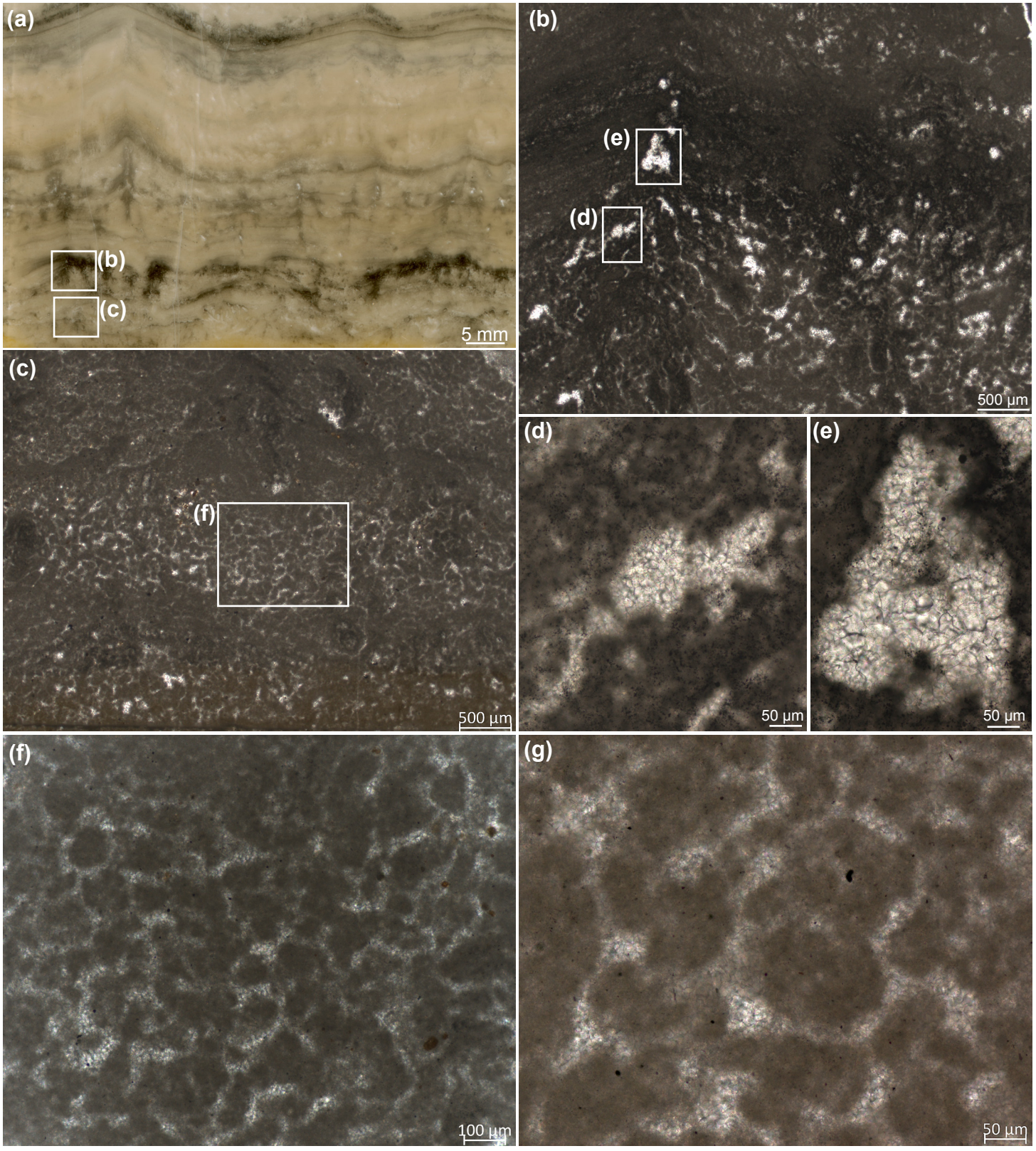

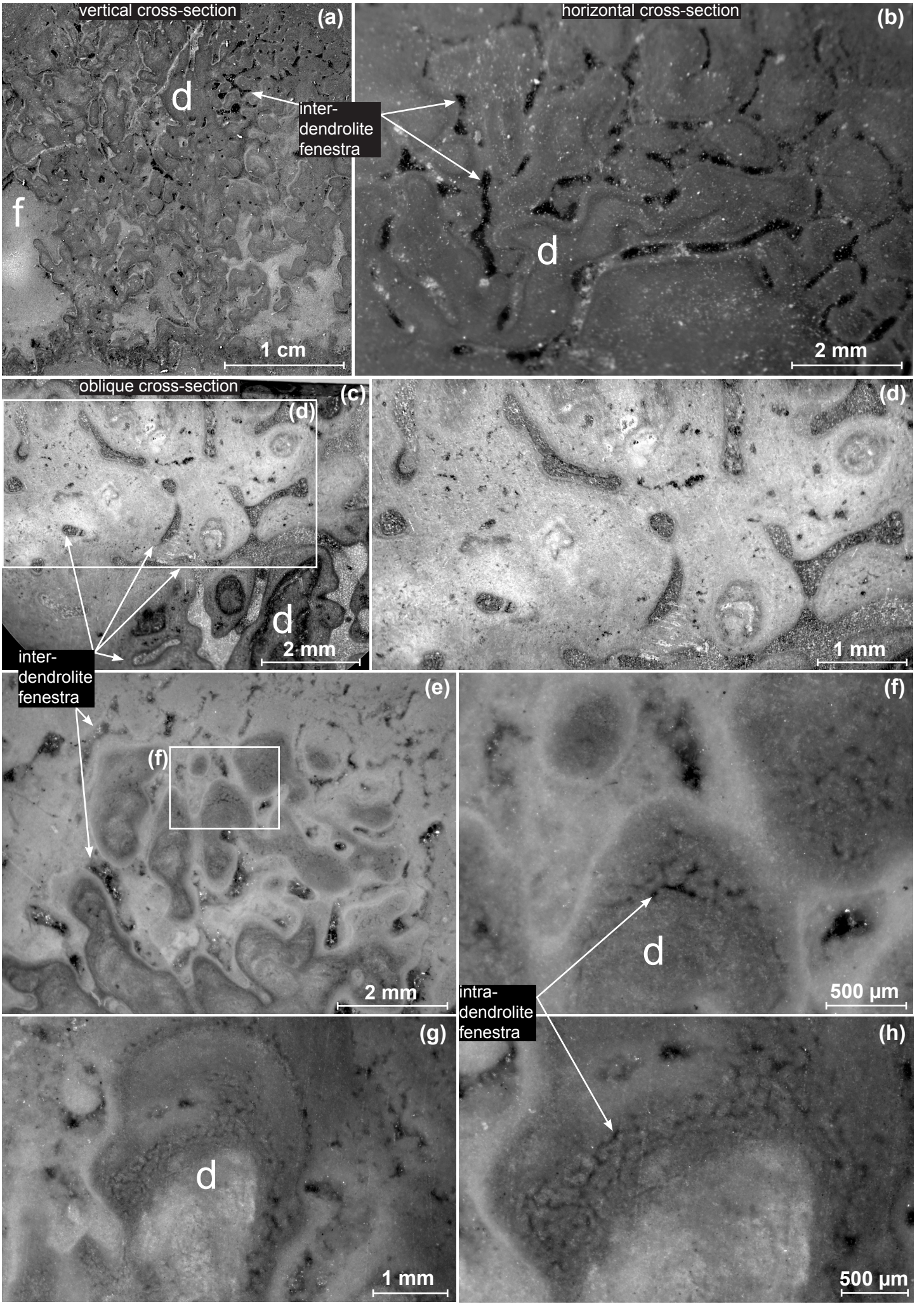
vertical cross-section
(a)
d
inter-
dendrolite
fenestra
f
1 cm
horizontal cross-section
(b)
d
2 mm
oblique cross-section
(c)
(d)
d
2 mm
inter-
dendrolite
fenestra
(d)
1 mm
(e)
(f)
2 mm
(f)
d
500 µm
intra-
dendrolite
fenestra
(g)
d
1 mm
(h)
500 µm

Figure 4

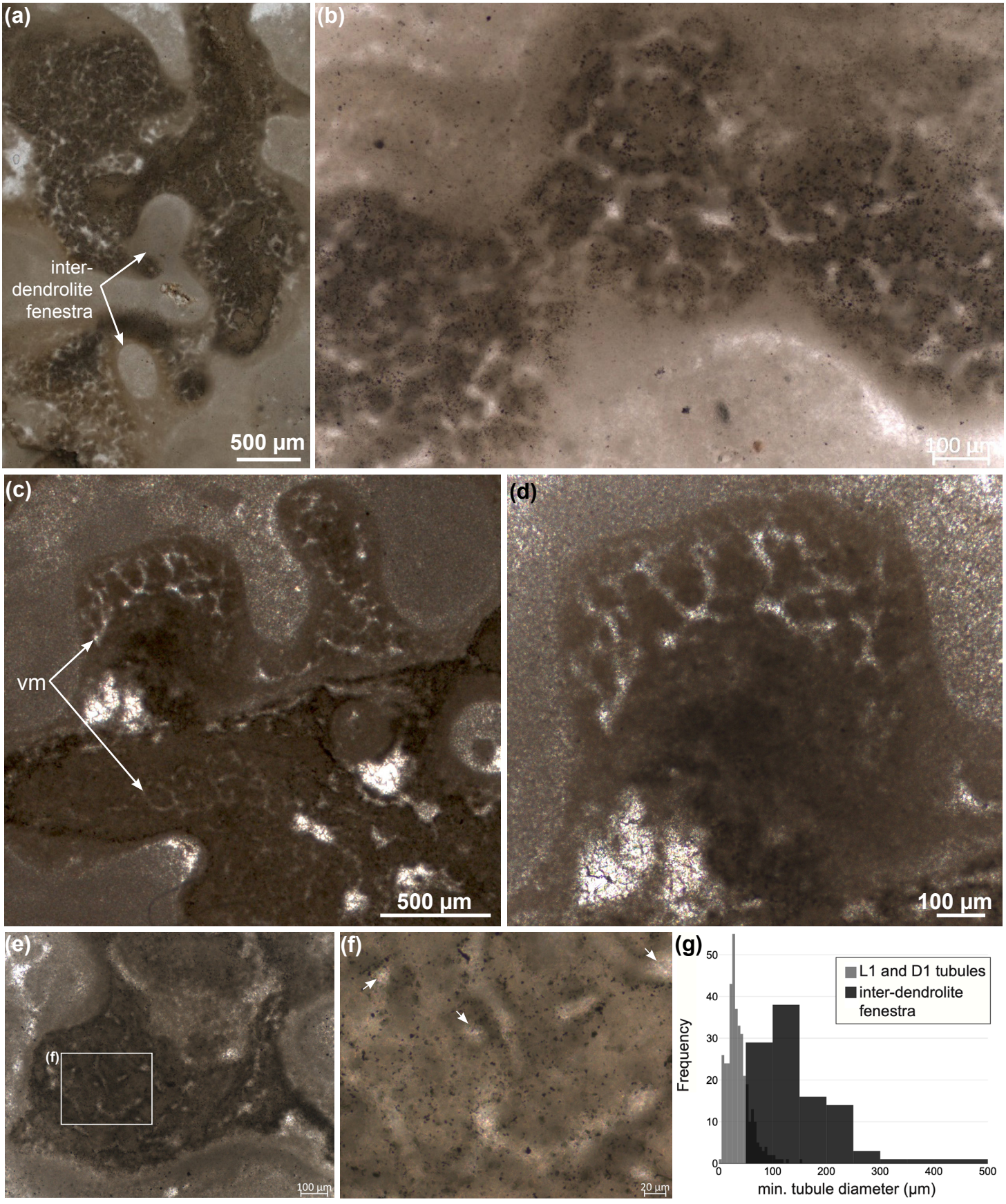
(a)
inter-
dendrolite
fenestra
500 µm
(b)
100 µm
(c)
vm
500 µm
(d)
100 µm
(e)
(f)
100 µm
(f)
20 µm
(g)
L1 and D1 tubules
inter-dendrolite
fenestra
Frequency
0
10
20
30
40
50
0
100
200
300
400
500
min. tubule diameter (µm)

Figure 5

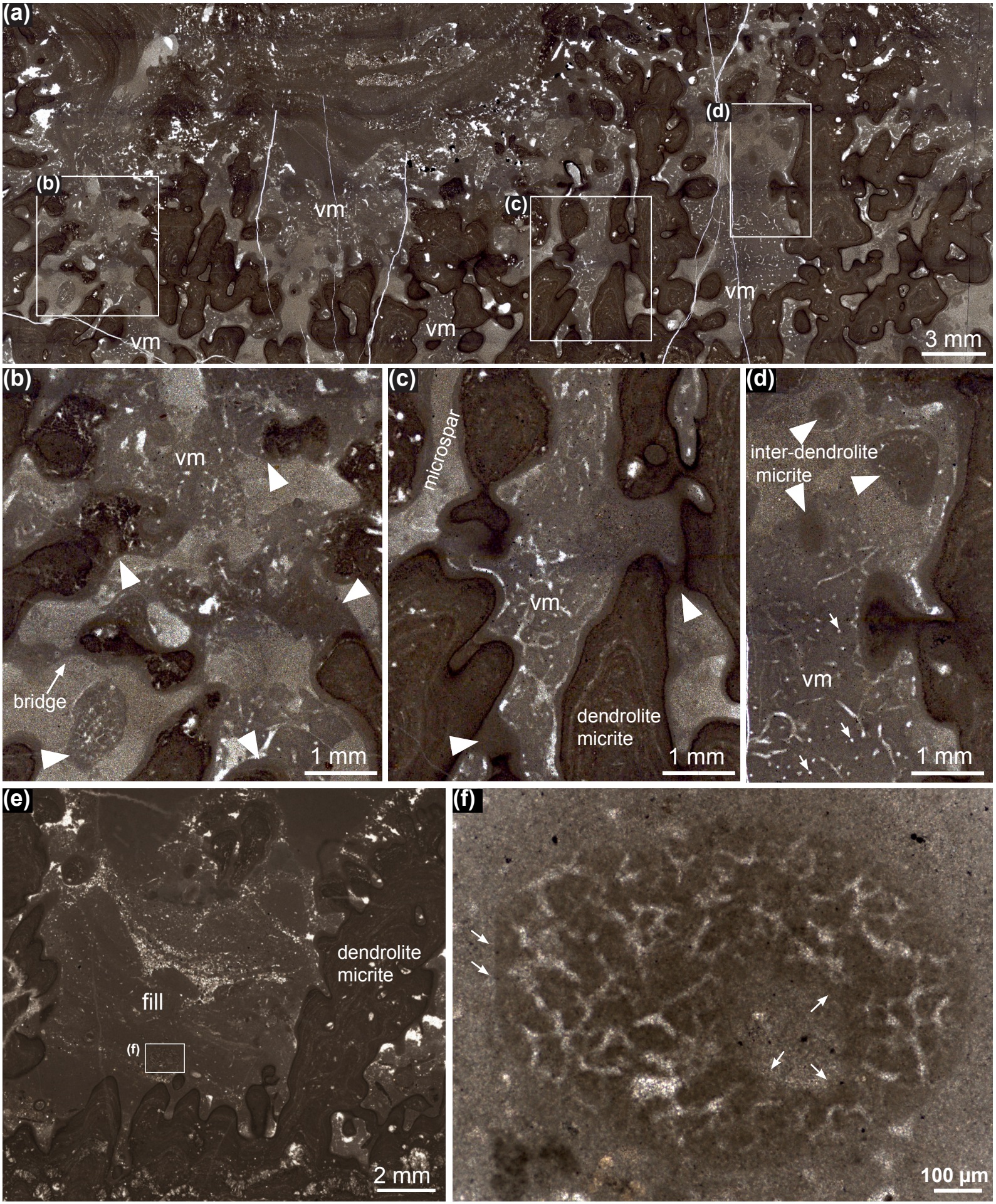
(a)
(b)
(c)
(d)
vm
vm
vm
vm
vm
3 mm
(b)
vm
bridge
1 mm
(c)
microspar
vm
dendrolite
micrite
1 mm
(d)
inter-dendrolite
micrite
vm
1 mm
(e)
dendrolite
micrite
fill
(f)
2 mm
(f)
100 µm

Figure 6

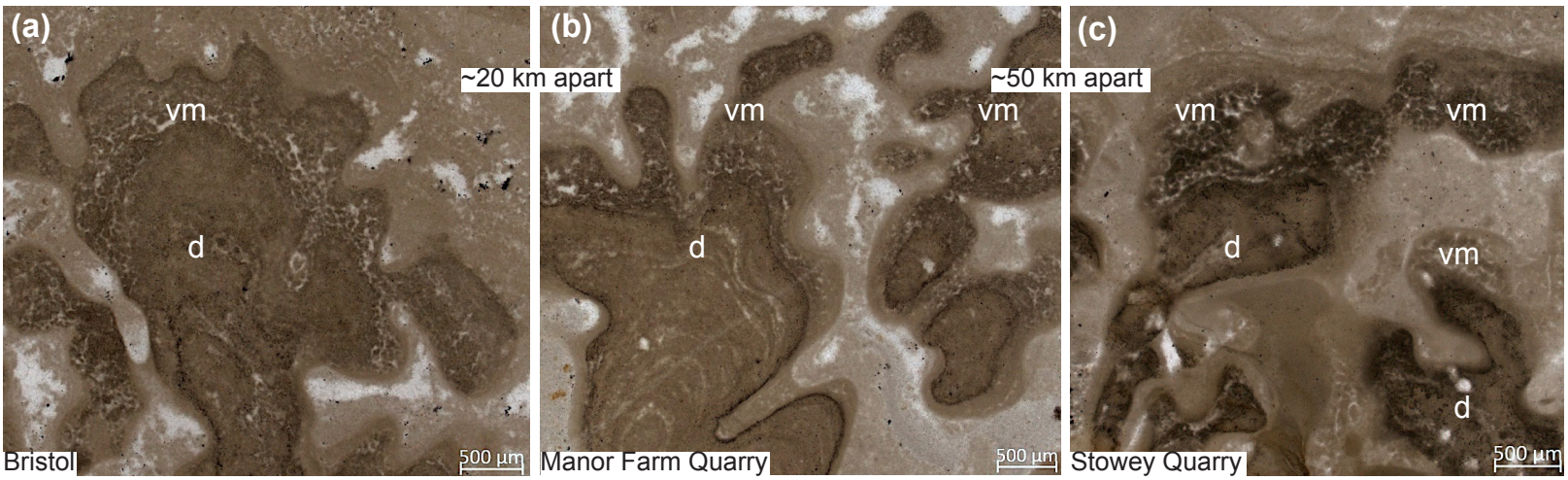
(a)
~20 km apart
vm
d
Bristol
500 µm
(b)
~50 km apart
vm
vm
d
Manor Farm Quarry
500 µm
(c)
vm
vm
d
vm
d
Stowey Quarry
500 µm

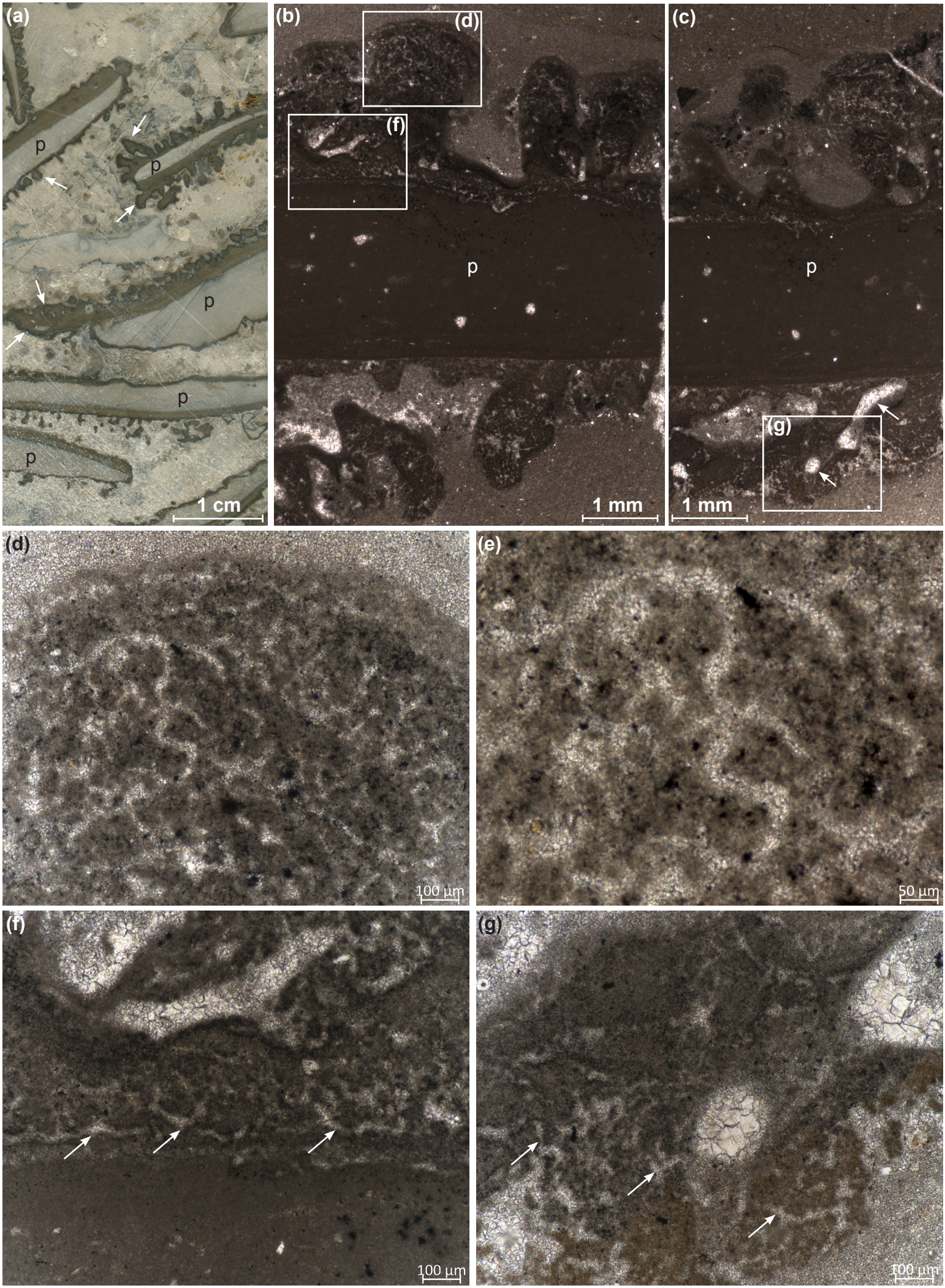
(a)
p
p
p
p
p
1 cm
(b)
(d)
(f)
p
1 mm
(c)
p
(g)
1 mm
(d)
100 µm
(e)
50 µm
(f)
100 µm
(g)
100 µm

Figure 8

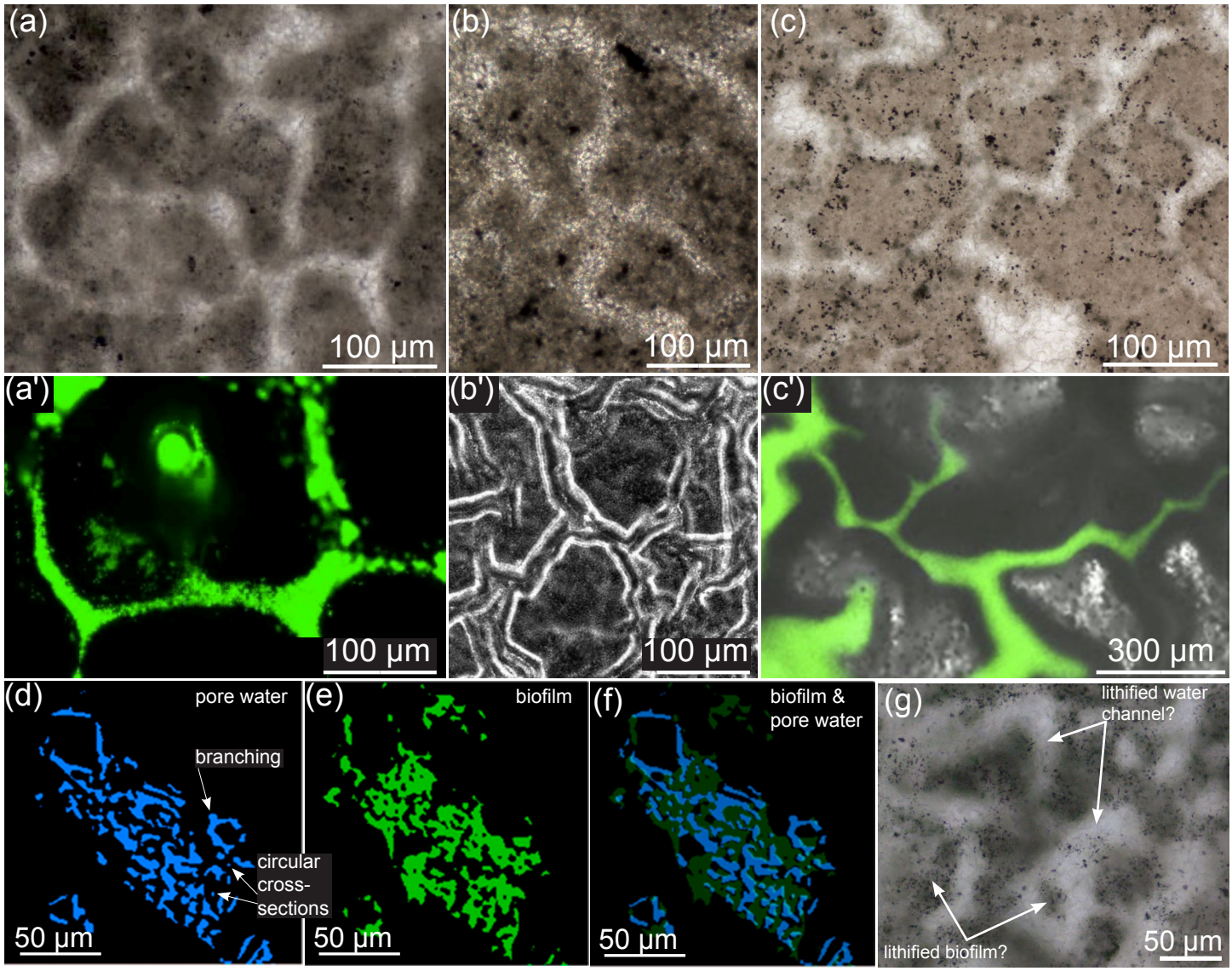
(a)
100 µm
(b)
100 µm
(c)
100 µm
(a')
100 µm
(b')
100 µm
(c')
300 µm
(d)
pore water
branching
circular cross-sections
50 µm
(e)
biofilm
50 µm
(f)
biofilm & pore water
50 µm
(g)
lithified water channel?
lithified biofilm?
50 µm

Figure 9

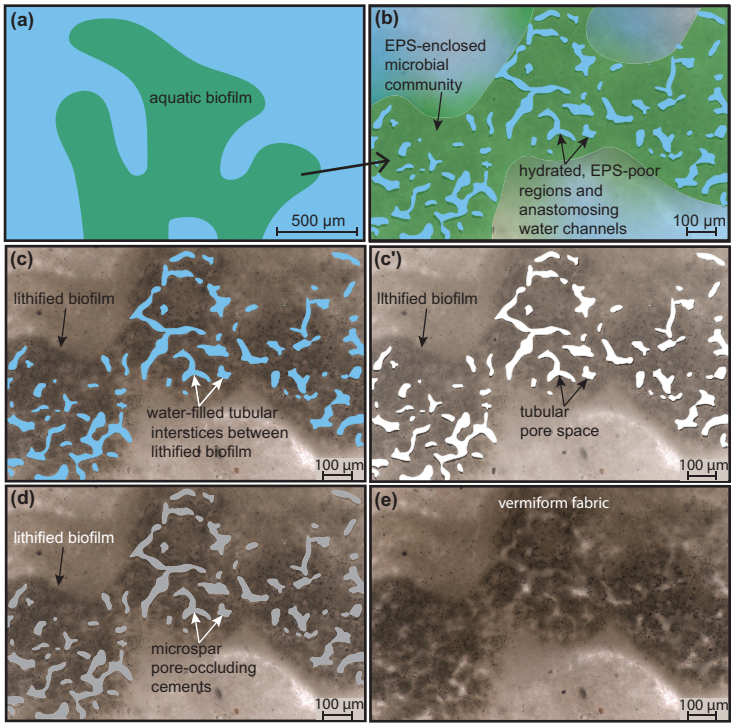

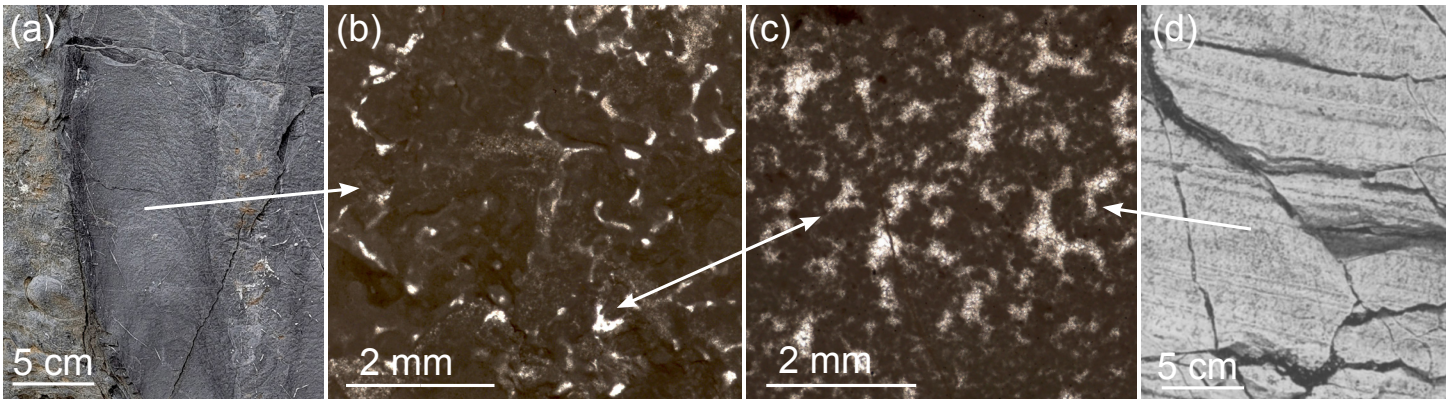

Figure 11

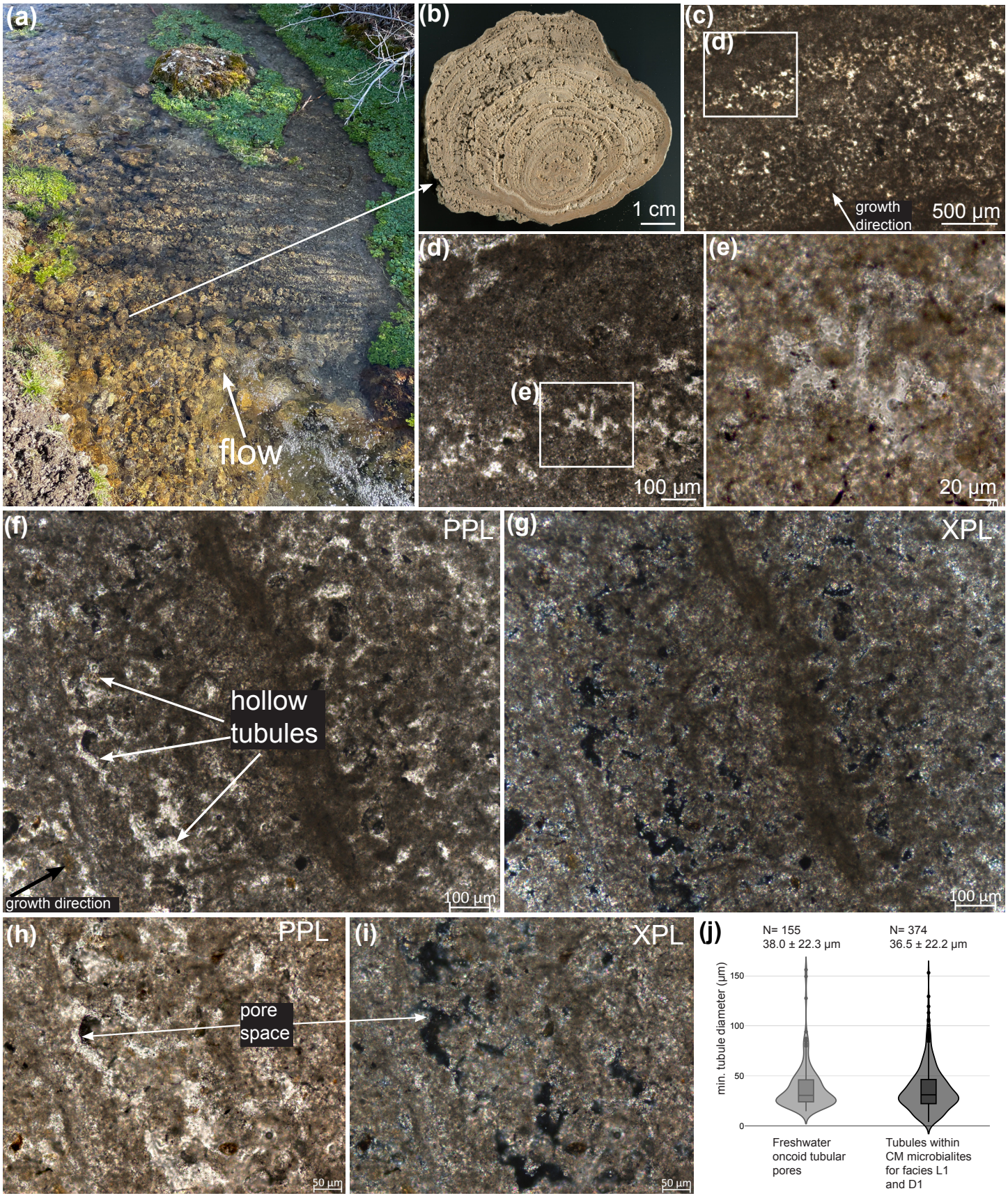
(a)
flow
(b)
1 cm
(c)
(d)
growth direction
500 µm
(d)
(e)
100 µm
(e)
20 µm
(f)
PPL
hollow tubules
growth direction
100 µm
(g)
XPL
100 µm
(h)
PPL
pore space
50 µm
(i)
XPL
50 µm
(j)
N= 155
38.0 ± 22.3 µm
N= 374
36.5 ± 22.2 µm
min. tubule diameter (µm)
150
100
50
0
Freshwater oncoid tubular pores
Tubules within CM microbialites for facies L1 and D1

Figure 10